SOLAR-GLIDING ARC PLASMA REACTOR FOR GAS PHASE CHEMICAL SYNTHESIS
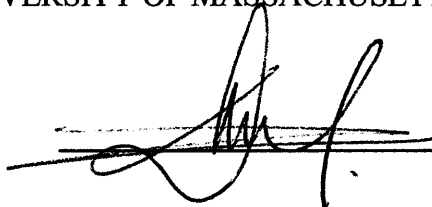
BY

DASSOU NAGASSOU

DIPLOME D'INGENIEUR DES TRAVAUX, ECOLE NATIONALE DES TRAVAUX
   PUBLICS DE NDJAMENA, CHAD (2000)
M.S. INTERNATIONAL INSTITUTE FOR WATER AND ENVIRONMENTAL
   ENGINEERING (2IE) OF OUAGADOUGOU, BURKINA-FASO (2010)

SUBMITTED IN PARTIAL FULFILLMENT OF THE REQUIREMENTS
FOR THE DEGREE OF DOCTOR OF PHILOSOPHY
ENERGY ENGINEERING
UNIVERSITY OF MASSACHUSETTS LOWELL

Signature of Author: _____ Date: _December 17th, 2018_

Signature of Dissertation Chair: _____
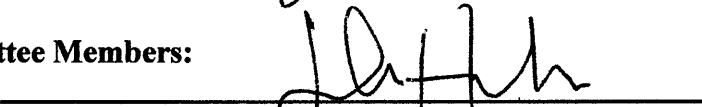Name: Prof. Juan Pablo Trelles

Signature of Dissertation Committee Members:
Committee Member Signature: _____
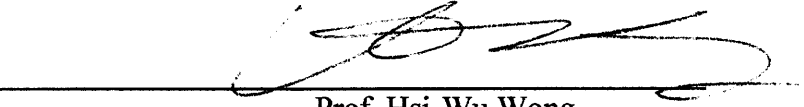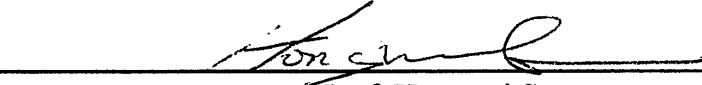Name: Prof. John Hunter Mack

Committee Member Signature: _____
Name: Prof. Hsi-Wu Wong

Committee Member Signature: _____
Name: Prof. Hongwei Sun

i

SOLAR-GLIDING ARC PLASMA REACTOR FOR GAS PHASE CHEMICAL SYNTHESIS

BY

DASSOU NAGASSOU

ABSTRACT OF A DISSERTATION SUBMITTED TO THE FACULTY OF THE
DEPARTMENT OF MECHANICAL ENGINEERING
IN PARTIAL FULFILMENT OF THE REQUIREMENTS

FOR THE DEGREE OF
DOCTOR OF PHILOSOPHY
ENERGY ENGINEERING
UNIVERSITY OF MASSACHUSETTS LOWELL
2018

Dissertation Supervisor: Juan Pablo Trelles, Ph.D.
Associate Professor, Department of Mechanical Engineering and Energy Engineering
Program

Abstract

The conversion of low-value feedstock such as carbon dioxide (CO_2) into higher-value products using renewable energy, particularly solar, can help fulfill the increasing need for fuels and chemicals while mitigating environmental emissions. This research explores the combined use of concentrated solar energy and nonequilibrium plasma (partially ionized gas) for sustainable chemical synthesis processes. Solar-plasma chemical synthesis seeks to exploit the sustainability advantages of the direct use of solar energy and the high efficiency and reliance on (potentially renewable) electricity of plasma processes. Two solar-gliding arc reactor configurations are investigated and evaluated for the decomposition of CO_2 at atmospheric pressure conditions, denoted as axi-radial (AXR) and reverse-vortex (RVX) flow. The former provides greater control of residence time but presents limited solar-plasma interaction; whereas the latter allows for greater interaction among solar photons and plasma electrons and excited species, but requires higher flow rates to confine the plasma, lowering the residence time. Evaluation of the plasma volume at different reactor orientations, aimed to mimic in-field operation, show that the AXR configuration leads to a larger plasma volume compared to that by the RVX design. Net-absorption tests at various radiation intensities, aimed to assess the extent of solar-plasma interaction, showed higher net-absorption for the RVX configuration than for the AXR. However, the AXR reactor leads to greater CO_2 decomposition mainly due to its flexibility in operating with lower residence times. The developed solar-gliding arc plasma reactor is evaluated following a systematic matrix experimentation approach to determine optimal operational characteristics and assess the overall performance of the solar-plasma chemical synthesis process.

Acknowledgements

I would like to thank the following people for their unwavering support and contribution to this work:

- ❖ My Advisor Prof. Juan Pablo Trelles who relentlessly work with me to instill the sense of academic rigor and excellence in all the facets of my research
- ❖ Prof. Hsi-Wu Wong for all the support in terms of laboratory measurement and instrumentation
- ❖ The committee members Prof. Hongwei Sun, Prof. Hsi-Wu Wong and Prof. John Hunter Mack for their valuable suggestions and guidance
- ❖ Dr. Maureen Howley for her endless support in chemical kinetics and analysis
- ❖ Prof. Shammy Shina for his coaching and support in design of experiment
- ❖ My colleagues in the Re-Engineered Energy Laboratory for their continuous support and assistance
- ❖ I would like to thank my wife Felicite and our children for their day-to-day support and prayers
- ❖ A special dedication to my mother Augustine Nelenang Nadjialndo and my father Nagassou Zozo
- ❖ I would like to extend my gratitude to my family members in Chad and elsewhere for their various encouragement during this journey

List of figures

List of tables

Nomenclature:

A_b: gas breakdown constant

AXR: Axi-radial reactor configuration

B_b: gas breakdown constant

C_p: specific heat

d_b: electrode spacing

D_a: aperture diameter

D_r: reactor cavity diameter

E_a: activation energy

h: convection coefficient

ΔH_r: enthalpy of the reaction

$\bar{I}_0$: time-averaged total incident solar radiation

$\bar{I}$: time-averaged incident solar radiation at exit

$I_{0,max}$: maximum incident solar radiation flux

L_8: orthogonal array matrix for 8 experimental runs

L_{16}: orthogonal array matrix for 16 experimental runs

L_r: reactor cavity length

m_{in}: mass at inlet

m_{out}: mass at outlet

$\dot{n}_{in}$: molar flow rate at inlet

$\dot{n}_{out}$: molar flow rate at outlet

Δn: population of activated complex

p: pressure

P_{solar}: power input from solar radiation

P_{plasma}: electrical power supply capacity

q_{cal}: heat flux (calorimeter)

Q_0: fraction of solar power

RVX: Reverse-vortex flow configuration

SEI: Specific Energy Input

T: temperature

$V_{b,max}$: power supply maximum voltage

V: volume

$\dot{V}$: volumetric flow rate

Greek letters

α: thermal diffusivity

γ: plate thickness

$γ_E$: secondary emission coefficient

ε: emissivity

$ρ_c$: density

μ: standard deviation of radial-mean

Θ: residence time

$η_a$: absorption efficiency

$η_c$: conversion efficiency

$η_e$: energy efficiency

Table of Contents

Chapter 1 Introduction

1.1 Background: Fossil Fuels and Renewable Energy

The world energy consumption continues to increase due to the utilization of fossil fuels as main energy sources (IEA, Annual Energy Outlook, 2017). The use of fossil fuels has led to a dramatic increase in carbon dioxide (CO_2) emissions, which is predicted to persist through the next few decades, as depicted in Fig. 1-1. The persistent discharge of CO_2 into the atmosphere will continue driving global climate change (Anderson et al., 2016). To mitigate this process, diverse approaches have been sought to reduce CO_2 emissions, including its sequestration and re-utilization; among them, the synthesis of chemicals from CO_2 feedstock is particularly appealing to offset emissions while fulfilling the increased need for fuels and chemicals.
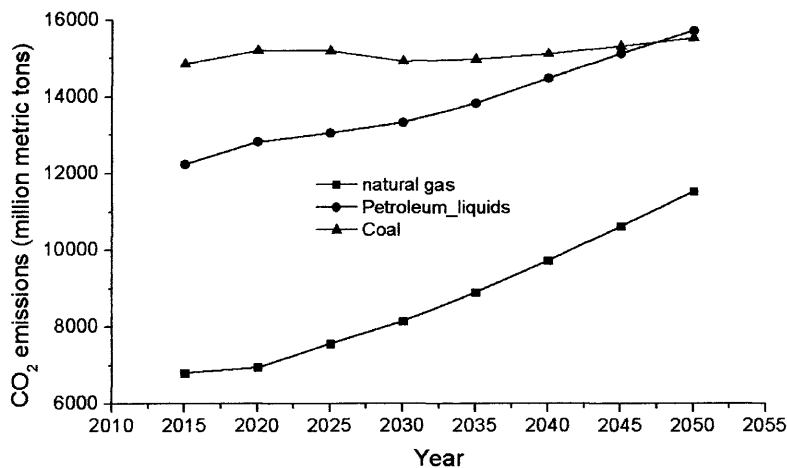
Fig. 1-1: Projected emissions of CO_2 by energy source: natural gas, coal, and petroleum (IEA, Annual Energy Outlook, 2017).

The amount of solar energy flux that reaches the earth surface is estimated to 1353 W/m² (Liou, 2002), largely surpassing human society's current and forecasted energy needs. Nevertheless, although solar energy is a freely available resource, its utilization at an industrial level faces challenges related to its intermittency and the efficiency of solar-driven processes. As a first step for solar energy utilization, solar radiation needs to be aimed towards a target-processing medium. Main approaches to concentrate solar irradiation are depicted in Fig. 1-2, namely parabolic troughs, dish collectors, and solar power towers. Concentrated solar power, due to its high energy densities (large radiative fluxes), is particularly suitable for the devising of high-throughput processes, including chemical synthesis.
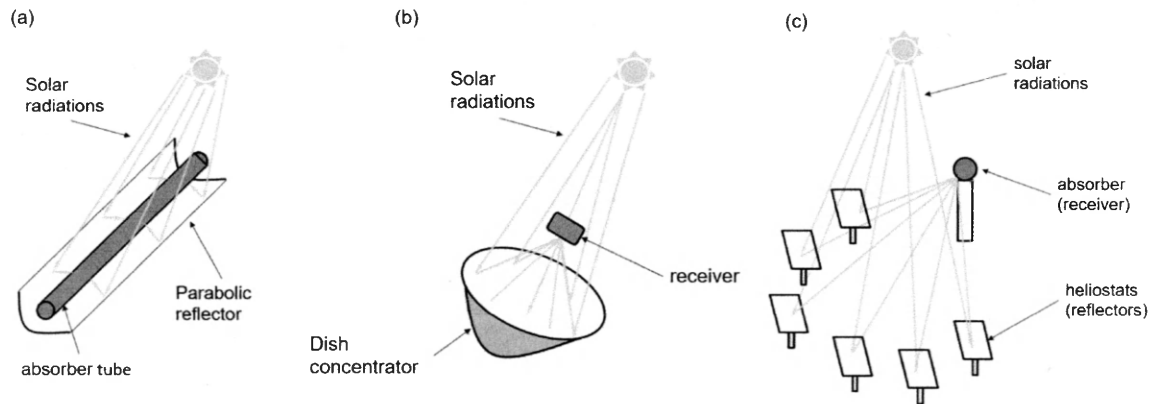
Fig. 1-2: Concentrated solar technologies: (a) parabolic trough, (b) dish collector, (c) solar tower.
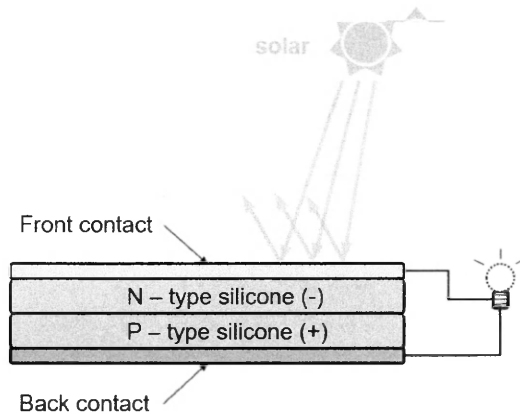
Fig. 1-3: Photovoltaic cell depicting its composition, two silicone semiconductor materials (of P and N type), the incidence of solar radiation, and the production of electrical energy.

Another established technology to harvest solar energy exploits the photovoltaic (PV) effect, which directly converts solar photons into electricity. Figure 1-3 shows the process of photo-generated potential difference using two silicone semiconductor materials (P and N type), which react to solar photons generating a potential difference and a net stream of electric current.

Plasmas, typically generated by electrical discharges, are ionized gases composed of charged particles (electrons, ions, excited atoms and molecules). The number of positive and negative charges balances each other making the plasma neutrally charged but remains reactive to electromagnetic fields (Chen & Smith, 2007). Plasmas can be found in natural and technological contexts, as depicted in Fig. 1-4, from aurora borealis and lightning bolts, to gliding-arc discharges and plasma-torches.
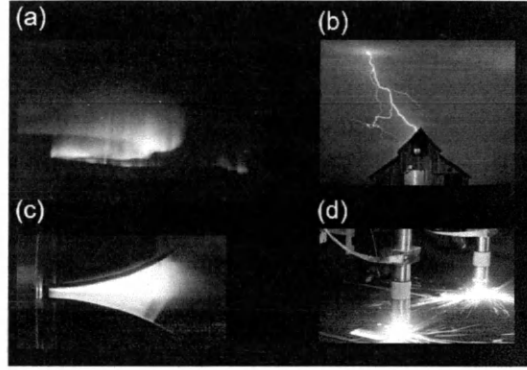
Fig. 1-4: Natural and technological plasmas: (a)[1] aurora borealis, (b) lightning bolt, (c) gliding arc discharge, and (d)[2] plasma torch for cutting and welding.

Plasmas are highly reactive due the molecular excitations promoted by charged particles, a characteristic that makes them particularly suited for chemical synthesis processes. Plasmas are traditionally classified among: thermal and non-thermal or nonequilibrium. Thermal plasmas are in a state of Local Thermodynamic Equilibrium (LTE), in which all constituent species can be characterized as having the same temperature. In contrast, non-thermal or nonequilibrium plasmas are in a state of non-local thermodynamic equilibrium (Non-LTE or NLTE), in which the free electrons present significantly higher temperature than that of the heavy-species (ions, atoms, molecules). Thermal plasma processes present high energy densities and resiliency, whereas non-thermal ones, high selectivity and chemical efficiency (Fridman et al., 1999).

---

[1] http://sciencenordic.com/tracking-earth's-magnetic-field-northern-lights
[2] https://www.messer-cs.com/us/processes/plasma-cutting/

16

solar

Plasma plume

Cathode + -

anode

Solar panel
(photovoltaic)
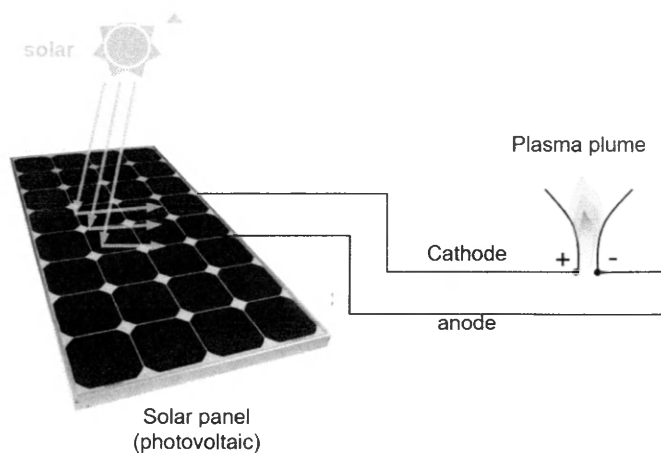
Fig. 1-5: schematic of a gliding arc discharge powered by a photovoltaic solar panel[3].

An especially important feature of plasma processes, in the context of sustainable chemical synthesis, is that they rely on electricity, which can be generated from renewable energy sources. For example, a solar PV system can be used to directly power an electrical discharge to generate plasma, as schematically depicted in Fig. 1-5.

1.2. Motivation: Solar Energy and Renewable Electricity for Chemical Synthesis

It is widely accepted that unchecked anthropogenic carbon dioxide (CO_2) emissions pose the imminent threat of irreversible climate change (Solomon et al., 2009). Additionally, natural gas, bolstered by shale gas reserves, is projected to continue to drive energy-related CO_2 emissions (EIA, Annual Energy Outlook, 2018). To address this compound challenge, diverse efforts to either capture or transform CO_2 into higher-value products are being sought (Abanades et al., 2014; Bohmer et al., 1991; Edwards et al., 1996). The direct use of solar energy for chemical fuel synthesis, in what are known as solar fuels, is seen as an appealing option to shift CO_2 emissions while addressing our pressing need for fuels. These processes can be mainly divided among solar thermochemical and photochemical. Alternatively, approaches that rely on electricity, which may not exclusively come from renewable sources, can be used for converting

---

[3] https://www.cleanenergyreviews.info/blog/best-quality-solar-panels-manufacturers

CO_2 into valuable products. Electricity-based chemical synthesis processes can be divided among electrochemical (liquid-phase) and plasma-chemical (gas-phase).

In solar thermochemical processes, concentrated solar radiation is channeled to a reactor to achieve high temperatures that drive chemical reactions (Abanades and Chambon, 2010; Hirsch and Steinfeld, 2003; Kodama, 2003; Roy et al., 2010). A major constraint of these processes is the need for high temperatures and advanced catalytic configurations to achieve suitable conversion efficiencies (Hirsch and Steinfeld, 2004). For instance, thermodynamic and chemical equilibrium considerations indicate that temperatures above 2700 °C are required to dissociate 50% of CO_2 in a direct single-step thermal process (Abanades and Chambon, 2010), whereas modern two-step thermal-cycling processes operate at temperatures of about 1600 °C (Chueh et al., 2010). Such high temperatures often lead to associated high cooling loads, stringent insulation requirements, and pronounced thermal stresses, which conduce to high equipment and process costs. Alternatively, the spectral characteristics of solar energy can be exploited for chemical synthesis via photochemistry. Photochemical processes involve the use of photocatalysts, such as titanium dioxide (TiO_2) or zirconium oxide (ZrO_2), to generate electron-hole pairs that drive electron-exchange catalytic reactions (Fujishima et al., 2000; Jin et al., 2014). Solar photochemical synthesis processes often operate with direct incident radiation and at lower temperatures, which can reduce equipment complexity and cost. Nevertheless, these low-intensity processes generally present limited throughput, which can limit their industrial viability (Roy et al., 2010).

In contrast to the direct use of solar energy, an inherently intermittent resource, the direct use of electricity, ideally from a combination of renewable energy sources such as solar photovoltaic or wind, for CO_2 decomposition can provide an alternative with the potential for continuous operation. Electrochemical processes involve a set of electrodes that deliver electricity through an electrolyte to drive reduction-oxidation reactions (Bogotsky, 2006). Electrochemical processes are employed in a wide range of applications, including the reduction of CO_2 into CO (Mohan, 2014; Oturan, 2014). Particularly, Shen and collaborators (Shen et al., 2015) studied the electrocatalytic reduction of CO_2 reporting 40% faradaic efficiency (efficiency with which electrons are

transferred to facilitate electrochemical reactions); whereas Hori and collaborators reported high CO_2 conversion, with up to 91% CO formation (Hori et al., 1987).

Plasma-chemical processes rely on electricity to generate plasma (partially ionized gas), leading to high gas-phase reactivity that drives chemical reactions (Fridman, 2008; Chen, 2016). Plasma can be generated through diverse means, such as electric arc, dielectric-barrier, spark, and microwave discharges (Fridman et al., 2011). The application of plasmas for chemical synthesis has a long trajectory (Fridman, 2008). Among plasma technologies for chemical syntheses, the gliding arc (glidarc) plasma source by Fridman and collaborators (Fridman et al., 1999) is particularly appealing due to its potential for resilient operation together with high energy efficiency. Nunnally and collaborators (Nunnally et al., 2011) investigated the effect of vortex flow in the dissociation of CO_2 in a glidarc plasmatron achieving 43% energy efficiency (Nunnally et al., 2011). Liu and collaborators devised a pulsed-power tornado glidarc reactor for CO_2 decomposition achieving 68% energy efficiency along with 22% CO_2 conversion (Liu et al., 2016). In contrast to electrochemical, plasma-chemical processes operate with gas-phase feedstock instead of liquid-phase media, a characteristic that can be appealing for the treatment of gaseous bi-products such as the flue gas from fossil fuel power plants.

Different combinations of the above approaches have been sought towards the aim of achieving higher efficiencies and/or greater operational advantages. For example, Wei and collaborators (Wei et al., 2014) devised a solar-photoelectrochemical cell that exploits vanadium photochemistry with the aim of splitting water for hydrogen production achieving 95% faradaic efficiency. Such approach relied on the intrinsic similarities between photochemical and electrochemical processes, such as their reliance on low-temperature liquid-phase processing media. In a similar manner, solar-thermochemical and plasma-chemical processes are somewhat compatible due to their operation with gas-phase reactants and at relatively high temperatures. The combination of solar-thermochemical and plasma-chemical processes has the potential to yield greater efficiencies and to alleviate the constraints imposed by the inherent intermittency of solar irradiation (Nagassou et al., 2017).

1.3. Goal and objectives

1.3.1. Goal

The aim of this research is to evaluate the combined use of concentrated solar energy and nonequilibrium plasma aimed to enhance the efficiency and resiliency of solar thermochemical synthesis processes.
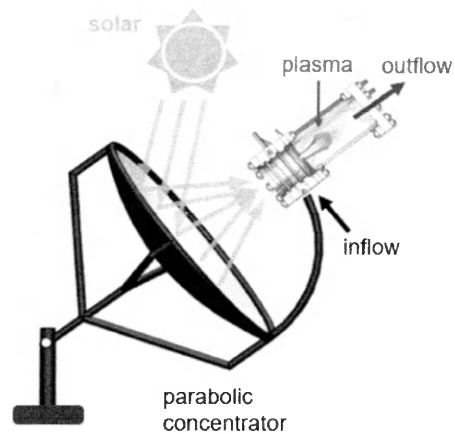
Fig. 1-6: Solar-plasma chemical synthesis concept.

Figure 1-6 depicts the conceptualization of the solar-plasma chemical process. A parabolic concentrator gathers and directs a solar radiation flux to a direct receiver-reactor fitted with a gliding arc discharge. The discharge is sustained by electricity, potentially solar photovoltaic or from another renewable source. A stream of feedstock gas is fed into the reactor, where the solar-plasma chemical synthesis process takes place, producing an outflow of gaseous products.

1.3.2. Objectives

Towards achieving the research goal, the proposed research has four main objectives:

1) Characterize a high-flux solar simulator for the evaluation of concentrated solar processes under laboratory conditions.

2) Design and build a direct solar-gliding arc plasma receiver-reactor for gas-phase chemical synthesis.

3) Characterize the design and operation of the solar-glidarc reactor in terms of plasma generation, solar-plasma interaction, gas transport, and chemical processing.

4) Investigate the effectiveness of the solar-glidarc reactor for the synthesis of chemicals via the processing of representative feedstock gases under atmospheric pressure conditions.

1.4. Significance

To combine the advantages of the solar energy resource and our electrical energy infrastructure, the evaluation of a solar-plasma receiver-reactor aimed for sustainable chemical synthesis, particularly the decomposition of undiluted gas-phase CO_2 and other low-value chemicals at atmospheric pressure conditions, will be performed. The reactor has the potential to enhance the efficiency of solar thermochemical processes and to mitigate their inherent intermittency by providing a means for continuous operation via electrical energy input. Two reactor configurations are introduced, namely reverse-vortex (RVX) flow and axi-radial (AXR) flow. The rationale and characteristics of both designs are presented, as well as their evaluation enhancing solar energy absorption and achieving CO_2 decomposition. Although a catalytic medium is used in most solar thermochemical reactors, no catalytic component is included in the presented reactors to isolate the role of the nonequilibrium plasma on the interaction of solar energy with the gaseous feedstock. (It is to be noted that in the absence of a catalytic medium, conventional solar thermochemical reactors are likely to produce negligible CO_2 decomposition.) The results suggest that solar-plasma receiver-reactors provide a compelling alternative for increasing the efficiency and reduce the intermittency of solar thermochemical processes.

Chapter 2 Solar simulator characterization

2.1. Solar simulator characterization

The characterization of a 6.5 kW xenon arc-lamp simulator was performed and sanctioned with the identification of the specific location of the focal point, the energy flux distribution, and the amount of power it delivers at the focal point (Bhatta et al., 2017).

The spectra of the sun (measured in Lowell, MA), the simulator xenon arc lamp and a metal halide lamp were measured using an AVASOFT 8 spectrometer with a wavelength ranging between 200 and 1100 nm are presented in Fig. 2-1. The results in Fig. 2-1 show that radiation from the simulator approximates that of the sun.
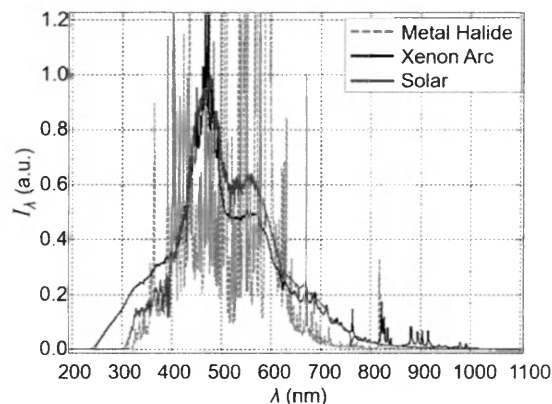
Fig. 2-1: Spectral characterization: normalized spectrum of solar energy (sun), the xenon short-arc lamp in the high-flux simulator, and a metal halide lamp.

The experimental set-up presented in Fig. 2-2 was used to determine the energy flux distribution produced by the simulator. The approach consists on taking images of

the reflected light from a plate placed at various location points along the axis. The images were analyzed through MATLAB image processing to determine the relative intensity of the incident radiation. Figure 3 shows the treatment of the images taken at different locations before and after the calculated focal point. The latter corresponds to the image that shows the least distortion in both horizontal and vertical directions.
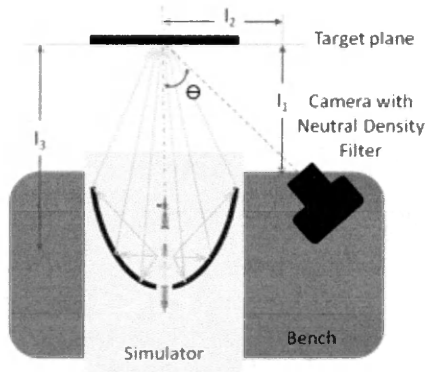
Fig. 2-2: Experimental set-up for flux intensity measurements.

| Focal - 2.6" | Focal - 1.6" | Focal | Focal + 1.6" | Focal + 2.6" |
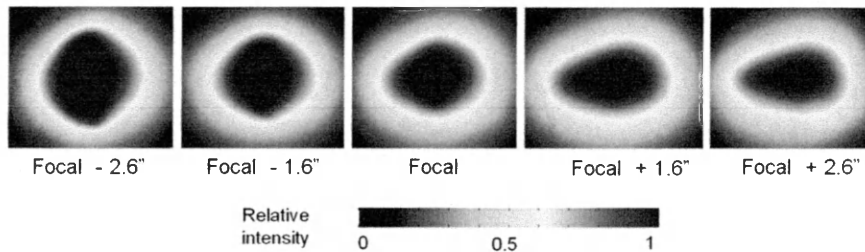
Fig. 2-3: Radiative intensity distribution maps at various locations before and after the estimated focal point.

To quantitatively determine the solar flux at the focal point, the same approach of image data collection and processing described above, was applied. To determine the intensity (magnitude) of the radiation flux, a black-painted copper disc of 15.2 cm diameter was placed at the identified focal location. In addition, an infrared thermometer was placed at the back of the plate to record temperature values along the radius, as depicted in Fig. 2-4.

23

The temperature distribution as a function of radial positions r in the calorimeter plate is recorded for each time interval Δt until steady state is reached. The temperature distribution through the plate (i.e. $T(r)$) is obtained by assuming rotational symmetry and using the energy balance along the plate given by:

$$\underbrace{\delta\rho_c C_p \frac{\partial T}{\partial t}}_{\text{transient}} - \underbrace{\frac{\delta}{r}\frac{\partial}{\partial r}(k_c r \frac{\partial T}{\partial r})}_{\text{conduction}} + \underbrace{2h(T - T_{amb})}_{\text{convection}} + \underbrace{2\varepsilon\sigma(T^4 - T_{amb}^4)}_{\text{radiation}} - \underbrace{\alpha q_{cal}}_{\text{incident flux}} = 0, \qquad (1)$$

where δ, ρ_c, C_p, ϵ, and σ are the plate thickness, density, specific heat, emissivity and Stefan-Boltzmann constant, respectively; and q_{cal} the heat flux on the calorimeter. The convection losses, given by the coefficient h and ambient temperature T_a, are determined experimentally during cooldown periods, given a value for $h \sim 9.11$ Wm^{-2}K^{-1}. Figure 5 shows the image processing and treatment to obtain the simulator flux.
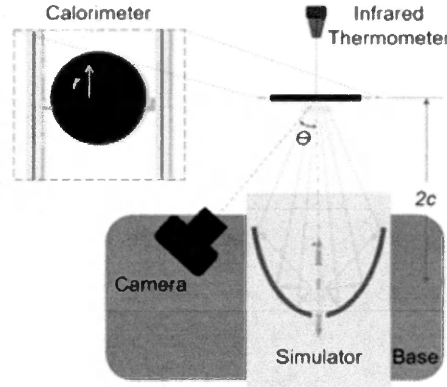
Fig. 2-4: Plate calorimeter experimental set-up for measuring high-flux solar radiation.

The total power deposited at the focal point was evaluated using:

$$\dot{Q}_{cal} = 2\pi \int_0^R q_{cal} r\, dr. \qquad (2)$$

where, q_{cal} is the flux previously determined. The average simulator energy flux is determined to be 270 Wm^{-2} and the total power is estimated to be 1.20 kW, which represents approximately 25% of the total simulator input power of 6.5 kW. The 1.20 kW

24

represent the maximum amount of solar radiation available as input into the solar-plasma reactor.
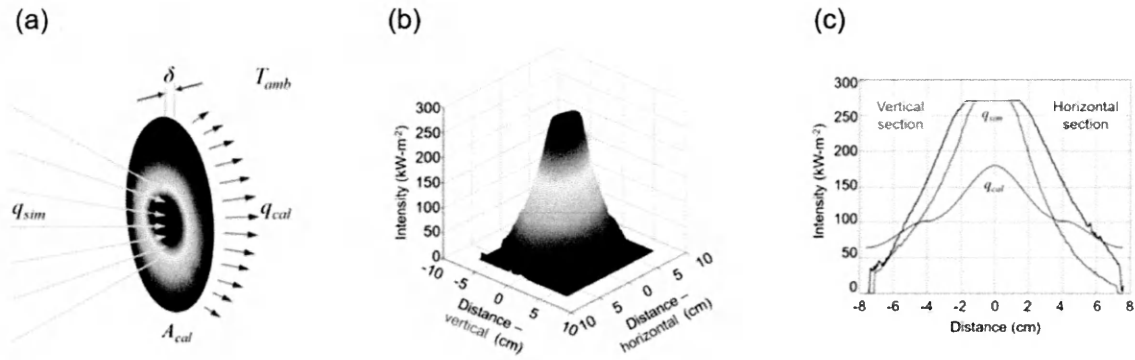
Fig. 2-5: Radiation flux characterization: (a) calorimeter energy balance, (b) isometric view of the intensity distribution, and (c) calibrated intensity distribution from the simulator.

Chapter 3 Solar- gliding arc reactor design

3.1. Design concept

The evaluation of the potential synergistic use of two sources of energy, i.e. solar and electrical, for chemical synthesis requires the definition of appropriate performance metrics. Three key performance indicators are used in the present work: (*i*) solar radiation absorption efficiency defined by:

$$\eta_a = \frac{\bar{I}_0 - \bar{I}}{\bar{I}_0},$$ (3)

where $\bar{I}_0$ is the time-averaged total incident solar radiation into the reactor chamber and $\bar{I}$ is the time-averaged radiation at the reactor's exit (after its interaction with the plasma); (*ii*) conversion efficiency:

$$\eta_c = \frac{\dot{n}_{in} - \dot{n}_{out}}{\dot{n}_{in}},$$ (4)

where n_{in} and n_{out} are the molar flow rate of feedstock (CO_2) at the inflow and outflow, respectively; and (*iii*) net energy efficiency, given by:

$$\eta_e = \frac{\Delta H_r}{SEI} \eta_c,$$ (5)

where ΔH_r is the heat of reaction necessary to decompose the feedstock molecules (280 kJ/mol for CO_2), and SEI the specific energy input given by:

$$SEI = \frac{P_{solar} + P_{plasma}}{\dot{V}},$$ (6)

where P_{solar} and P_{plasma} are the power input from solar radiation (i.e. total incident radiation $\bar{I}_0$ times receiver area) and consumed by the plasma (provided by the electric power supply), respectively; and $\dot{V}$ the volumetric flow rate of the feedstock. Notice that

Eq. (6) can be used to assess solar-thermochemical and plasma-chemical processes (i.e. by setting P_{plasma} or P_{solar} equal to zero in Eq. (6), respectively), yet it provides an inadequate assessment of the reactor performance given the intrinsically different nature of the energy inputs (e.g. whereas electricity consumption is an operational cost, the required radiation influx determines the capital cost of the heliostat field or solar concentrator).
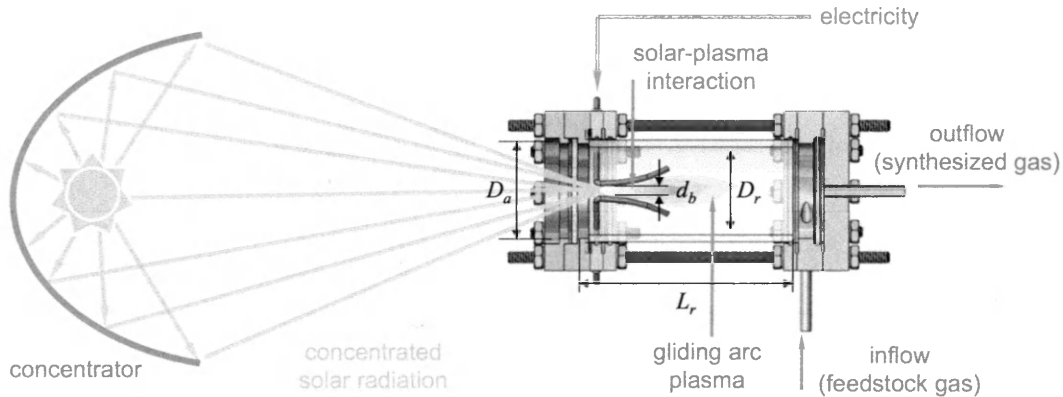
Fig. 3-1: Solar-plasma reactor concept: schematic depicting the concentrated solar energy influx, the direct solar-glidarc receiver-reactor, solar-plasma interaction inside a reactor cavity, and the conversion of the feedstock gas into synthesized gas.

The design concept of a solar-plasma reactor based on a direct-receiver chamber and a gliding arc discharge is presented in Fig. 3-1. The reactor design aims to maximize solar-plasma interaction as well as plasma-gas interaction. The former can lead to greater enhancement of the CO_2 decomposition process (e.g. by photon absorption of excited species from the plasmas), whereas the latter ensures the processing of a greater amount of feedstock (Nagassou et al., 2017). Figure 3-1 shows the channeling of concentrated solar radiation (e.g. from a parabolic concentrator or a heliostat field) passing through the receiver window and merging into the focal point located inside the reactor. The focal point is placed in the middle of the diverging electrodes where a gliding arc (glidarc) discharge is sustained by input electric power. The reactor aims to the conversion of the gas-phase feedstock into a synthesized outflow gas stream due to its interaction with the

concentrated solar radiation flux and the glidarc discharge. Key reactor design parameters are the diameter of the solar influx aperture D_a, the diameter D_r and length L_r of the reactor chamber, and the inter-electrode spacing d_b; the design criteria for sizing these are described next.

3.2. Design criteria

The design and sizing of the reactor follows three main criteria, namely: solar-plasma interaction, formation and control of the plasma, and residence time of the gaseous feedstock.

3.2.1 Solar-plasma interaction

Two key parameters drive the solar-plasma interaction: the receiver aperture and the location of plasma formation. The former determines how much solar radiation reaches the inside of the reactor cavity and where this radiation reaches its maximum (i.e. at the focal point), while the latter determines the point of expected maximum solar-plasma interaction.

The size of the aperture is determined following the work of Steinfeld and collaborators (Steinfeld et al., 1998) as:

$$D_a = 2\left[-2\mu^2 \ln\left(1 - \frac{Q_0}{2\pi\mu^2 I_{0,\max}}\right)\right]^{\frac{1}{2}}, \tag{7}$$

where Q_0 is the fraction of solar power required at target; μ is the standard deviation of the radial-mean in the Gaussian approximation of the solar flux distribution, and $I_{0,\max}$ is the maximum incident solar radiation flux. The sizing of the receiver aperture, i.e. the value of D_a, depends on the characteristics of the solar radiation source. In the present work, the radiation source is a 6.5 kW high-flux solar simulator whose performance features have been previously determined (Bhatta et al., 2016). For this solar simulator, the peak solar power at the focal point was estimated equal to 1.20 kW, with $I_{0,\max}$ = 270 kW-m^{-2} and μ = 0.06 m. Setting Q_0 to 80% capture of the peak solar power received

28

inside the cavity, i.e. $Q_0 = 0.96$ kW, gives an approximated value of D_a of ~ 70 mm, which is used in the reactor implementations.

The location of plasma formation in the context of a glidarc discharge corresponds to the minimum inter-electrode spacing, where electric breakdown occurs (discussed in the next section). The focal point is placed 60 mm behind the quartz window aperture, inside the reactor-cavity. The location of minimum inter-electrode distance is set 20 mm before the focal point. This location is set such to favor the interaction between the concentrated solar radiation influx and the electric arc as it glides downstream along the electrodes during each gliding cycle.

In addition to the receiver aperture and location of plasma formation, the solar radiation-plasma interaction depends on the characteristics of the interior of the chamber. The inner surface of the chamber is fitted with a quartz cylinder to limit surface deposition. The cylindrical quartz surface can be covered with a highly reflective surface to promote greater probability of interaction of solar radiation with the plasma volume (via multiple reflections) or with a thermal insulation layer to limit energy losses. The former option is adopted in the design implementations presented in Section3.3.3. Additionally, for the characterization experiments described in Section 3.4.2, no coverage of the quartz cylinder is employed such to have clear optical access into the chamber.

3.2.2 Plasma formation

The formation of the volume of plasma in a glidarc discharge depends on the inter-electrode spacing and the electrodes shape and configuration. The inter-electrode spacing needs to be such to allow electric breakdown for the initiation of the arc given the aimed feedstock gas and maximum voltage of the power supply. An additional design constraint in solar-glidarc reactors is that, while most glidarcs have a planar configuration (i.e. the electrodes are aligned along a single plane, see e.g. (Fridman et al., 2011), the incoming radiation flux has a conical profile. Such geometric mismatch would lead to inadequate solar-plasma interaction. The reverse-vortex glidarc configuration developed by Fridman and collaborators (Fridman et al., 1999) provides a cylindrical plasma volume more suitable for solar-plasma interaction, yet the plasma is concentrated along a

cylindrical surface (promoted by a spiral electrode) rather than in its core. In the present work, a three-electrode configuration (two powered and one ground) forming an equilateral triangle and powered by two power supplies connected in parallel was devised. This configuration is more effective when powered by alternating-current (AC) high-voltage power supplies and leads to the generation of a Y-shaped arc within the inter-electrode region. Details of the electrode configuration are presented in Section 3.3.3 and of the formed plasma in Section 3.4.2.

The minimum inter-electrode distance, defined as the breakdown distance d_b (size of the sides of the triangular inter-electrode section), is estimated using Paschen's law (Massarczyk et al., 2016) as:

$$\frac{B_b p d_b}{\ln(A_b p d_b) - \ln(\ln(1 + \gamma_{se}^{-1}))} - V_{b,\max} = 0, \tag{8}$$

where A_b and B_b are gas breakdown constants specific to carbon dioxide (Burm, 2007), p is pressure (set equal to atmospheric pressure), and γ_{SE} is the secondary emission coefficient for the electrode material (set to 0.01 (Burm, 2007) for copper in the present reactor implementations), and $V_{b,\max}$ the maximum voltage from the power supply. For a maximum voltage of 20 kV used in the present investigation, d_b is ~ 5.10 mm, a value consistent with that used by Taylan and collaborators for an atmospheric pressure CO_2 plasma (Taylan et al., 2013). Equation (8) is valid for direct-current (DC) electric power input. The use of AC power supplies (20-60 kHz adjustable frequency, 120 W maximum power each) allows a greater d_b, which is chosen equal to 6.0 mm in the reactor implementations in Section 2.3. Off-solar tests confirmed that no breakdown was achieved for d_b equal 7.0 mm and above.

Finally, the characteristics of the glidarc arc plasma depend on the shape of the electrodes. The electrodes are shaped with a main radius of curvature of 114.3 mm, which aims to ensure smooth gliding and appropriate extent of the formed arc.

3.2.3 Residence time

The residence time θ is a function of the reactor volume, defined by the reactor diameter D_r and length L_r, and the volumetric flow rate $\dot{V}$. The reactor cavity diameter

D_r is constrained to be slightly larger than D_a to maximize the solar influx and minimize radiation losses. Moreover, the sizing of D_r and of L_r has to take into account the extent of the curved electrodes to prevent electrical contact. The residence time for given $\dot{V}$, D_r and L_r is given by:

$$\theta = \frac{\pi D_r^2 L_r}{4\dot{V}}.$$ (9)

Based on Eq. (9), low volumetric flow rates favor high residence times. Nevertheless, the magnitude of flow rate has important implications on plasma formation and stability, as discussed in Section 4. For both reactor implementations in Section 2.3, the diameter of the reactor chamber D_r is set to 76 mm and its length L_r to 150 mm.

Preliminary designs were based on flow rates $\dot{V}$ of 4, 6, and 8 slpm, corresponding respectively to 10.25, 6.84, and 5.13 s of residence time. Experimental results revealed that flow rates up to 15 slpm, corresponding to 2.74 s of residence time, were required for proper confinement of the plasma under different reactor orientations.

3.3. Solar-glidarc reactor implementations

3.3.1. Design configurations

The solar-plasma reactor concept is implemented into the two reactor configurations depicted in Fig. 3-2, namely: axi-radial (AXR) and reverse-vortex (RVX) flow. The axi-radial flow design in Fig. 3-2 (a) offers relatively independent control of residence time (i.e. the length of the chamber is a relatively free design and operation parameter) but presents limited effectiveness of solar-plasma interaction given that the perforated quartz plate inside the reactor used to direct the stream of gas to the inter-electrode region limits the solar influx. In contrast, the reverse-vortex flow design produces better confinement of the plasma thanks to the formation of a reverse (interior) vortex flow, promoting solar-plasma interaction; but its adequate operation relies on having a high enough flow rate, which necessarily limits the allowable residence time of the processed gas. The above-described design and operation characteristics are evaluated in the following sections.
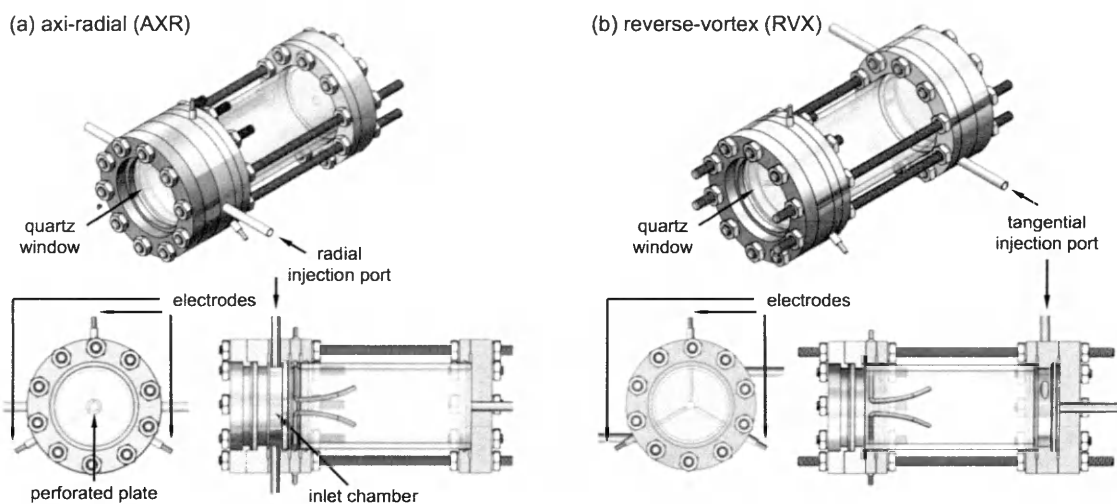
Fig. 3-2: Solar-glidarc reactor design configurations: (a) axi-radial (AXR) and (b) reverse-vortex (RVX). Isometric and side views of the reactors indicating the quartz window (receiver aperture), the set of three electrodes, and the gas injection ports for each configuration.

The two reactor configurations in Fig. 3-2 share the same key geometric parameters, i.e. aperture diameter D_a, reactor chamber diameter D_r and length L_r, and inter-electrode spacing d_b. The main difference between the AXR and RVX reactor configurations is the gas inflow system. The gas inflow is responsible of providing adequate confinement/gliding of the formed arc plasma. Additionally, the inflow gas system is designed such to flush the quartz window aperture in order to limit deposition of gaseous or particulate products (Kogan and Kogan, 2002).

The AXR design has two radial injection ports placed opposite to each other and near the quartz window. The inflow is confined by the quartz window from one end and by a perforated quartz plate from the other. The main function of the plate is to direct the radially-injected flow into the inter-electrode region to glide the arc. Additionally, the perforated plate creates an inlet chamber that confines the injected gas that limits back flow and hence the possibility of deposition of gaseous products. Given that the perforated plate helps direct the stream of feedstock gas directly into the plasma, the dynamics of the plasma is relatively independent of the reactor chamber length L_r (as

long as it does not interfere with the electrodes nor the plasma). Nevertheless, as described earlier, the perforated plate is in the field of view of the incident solar radiation, and hence limits its interaction with the plasma.

In contrast to the AXR design, the RVX design counts with radial injection ports placed at the reactor end opposite to the aperture. Such inflow system aims to produce a well-defined vortex flow along the inner surface of the reactor chamber that evolves towards the quartz window. The impinging flow flushes the quartz window with fresh feedstock, limiting deposition of reaction products, and returns following also a spiral motion confined within the core of the cylindrical chamber. Such flow configuration is commonly known as reverse-vortex (Kalra et al., 2005). The analysis of the inflow system for the RVX and AXR configurations is described next.

3.3.2. Flow path analysis

Understanding how the flow field behaves inside the cavity, particularly at the vicinities of the electrode boundaries, is crucial to determine how the flow will drive the gliding of the arc plasma, and hence its interaction with solar radiation. To ascertain that the selected dimensions of the reactor designs deliver optimal conditions for the plasma and solar radiation to interact effectively, Computational Fluid Dynamics (CFD) models of both reactor configurations were created using SolidWorks Flow Simulation (Dassault Systèmes, 2016) for the representative flow rates of 4, 6, and 8 slpm.

Results for the RVX configuration are shown in Fig. 3-3. The inflow from the back of the reactor cavity in this configuration generates a swirl flow along the reactor cavity's surface, which gets converted into a tornado flow (vertical flow with varying diameter) after reaching the aperture. The tornado rotates in the opposite direction of the main outer vortex and directs the flow towards the reactor cavity's outlet, pushing the plasma upwards. Figure 3-3(a) shows representative streamlines depicting the formation of the outer vortex and inner tornado. The strength of the inner tornado, which glides the arc plasma, increases with increasing flow rates, as indicated by the results in Fig. 3-3(b-d)).

33
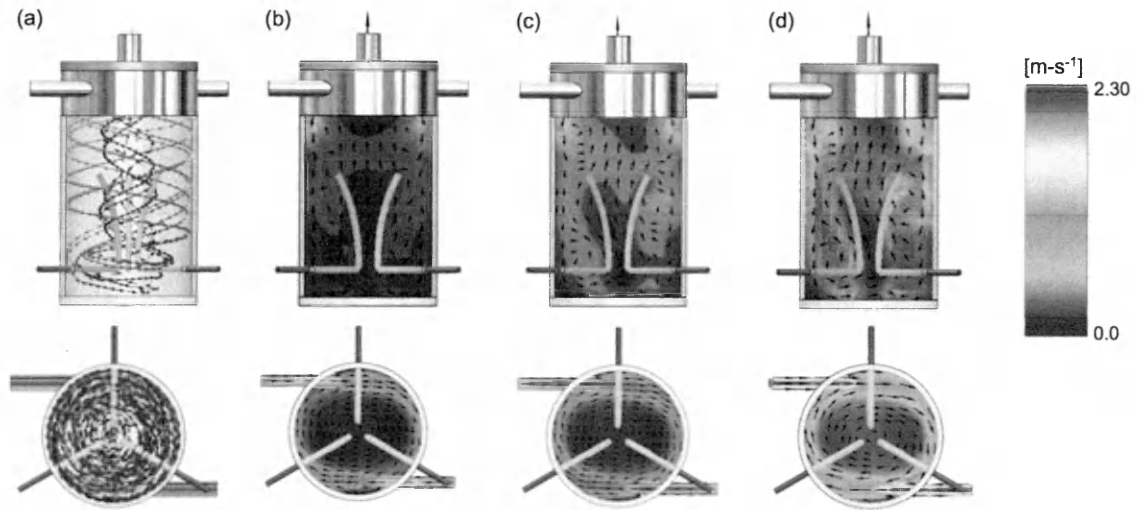
Fig. 3-3: Reverse-vortex flow: (a) representative streamlines and flow distributions for flow rates of (b) 4, (c) 6, and (d) 8 slpm; (*top*) side view and (*bottom*) top view across the axial mid-plane.
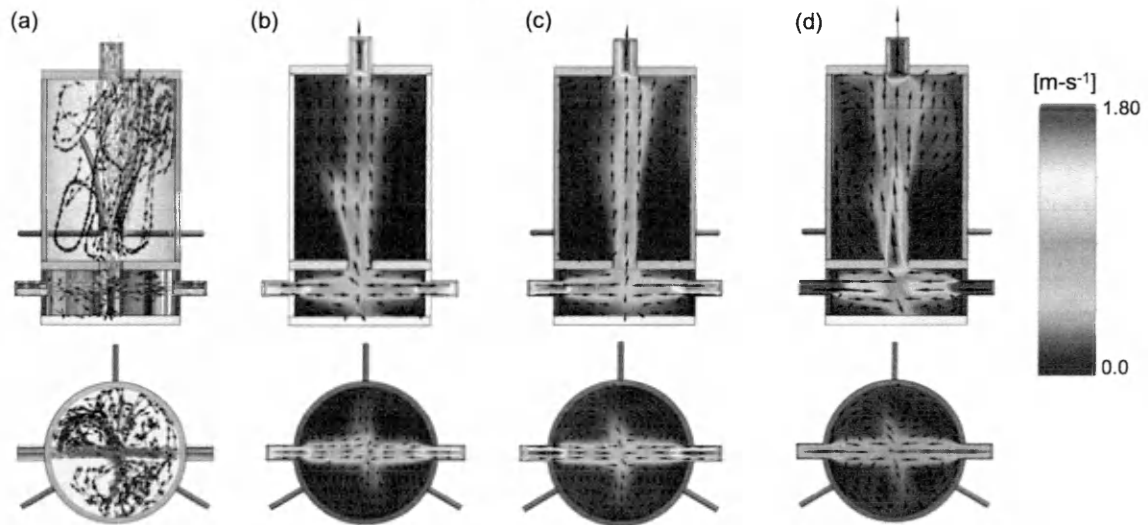
Fig. 3-4: Axi-radial flow: (a) representative streamlines and flow distributions for flow rates of (b) 4, (c) 6, and (d) 8 slpm; (*top*) side view and (*bottom*) top view across the axial mid-plane.

Results of the flow field through the AXR flow configuration are shown in Fig. 3-4. The AXR flow design is motivated by the possibility to de-couple the gliding of the arc by the flow from the residence time. A perforated quartz-disc acts as a flow-guide to deliver the gas to the inter-electrode region, where the plasma is generated. Figure 3-4(a) shows streamlines from the flow inlet, through the inlet chamber, and passing through the inter-electrode region in a focused manner thanks to the flow-guide disc. The results in Fig. 3-4(a) also show the formation of eddies at the end wall due to the impingement of the jet flow from the perforated plate. Figures 3-4(b-d) indicate an increased velocity field with increasing inlet flow rate.
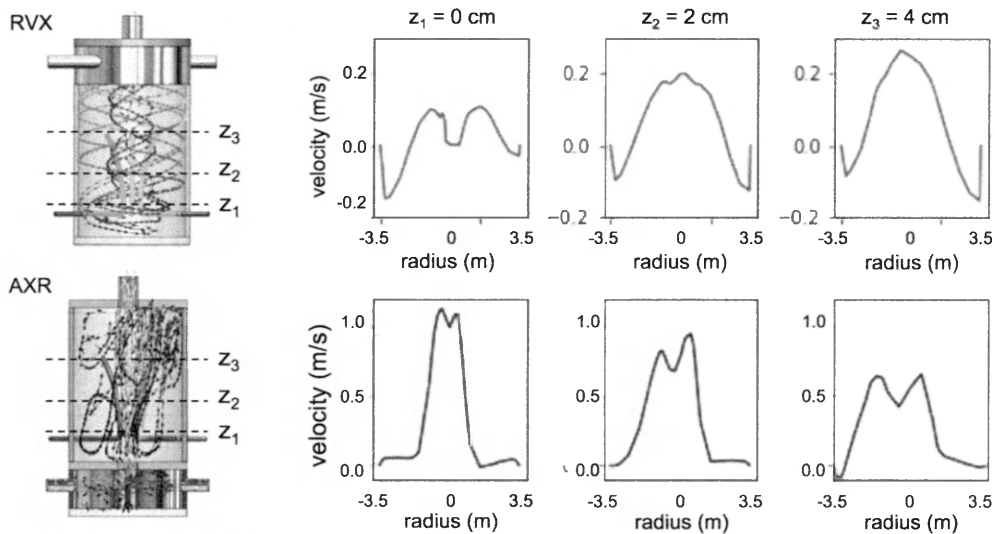
Fig. 3-5: Flow trajectories and velocity profiles for the (*top*) RVX and (*bottom*) AXR configurations. Axial velocity profiles at three axial (z) locations for 8 slpm flow rate: 0 (electrode entrance level), 2 and 4 cm.

Velocity profiles at different axial locations for 8 slpm and for both configurations are shown in Fig. 3-5. Although both configurations were able to deliver a velocity-lift at the center of the electrodes (aimed to push the electric arc), their magnitudes differ by a factor of 2.0; the axi-radial flow configuration delivers more accurately the gas flow at the eye of the inter-electrode region and at higher velocities. These results are consistent with experimental findings presented in later Sections 3.4.2 and 3.4.3.

35

3.3.3. Fabrication

The implementation of the two reactor configurations, AXR and RVX, are presented in Fig. 3-6. Given the relatively low temperatures of the processes aimed (compared to typical solar thermochemical processes), the flanges are made of stainless steel. Also, given the low-power nature of the gliding arc plasma, the electrodes are made of copper, and are insulated from the steel flanges through concentric machinable ceramic tubes.
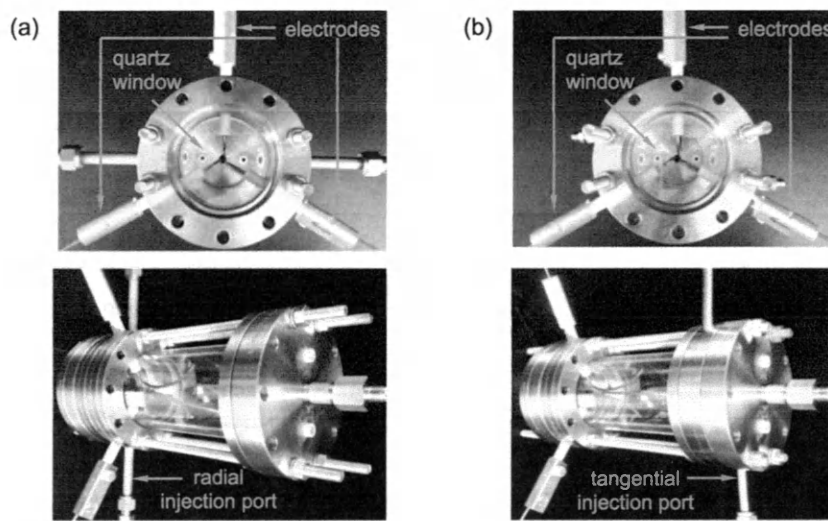
Fig. 3-6: Solar-glidarc reactors: (a) axi-radial (AXR) and (b) reverse-vortex (RVX).

Chapter 4 Solar-gliding arc plasma reactor characterization

4.1. Experimental set-up

The experimental set-up to characterize the solar-glidarc reactors is shown in Fig. 4-1. The feedstock gas is carbon dioxide. The solar-simulator is placed in front of the reactor along a horizontal line of sight. The product gases are collected at the exit for composition analysis. A quenching chamber to prevent gas-product recombination is placed downstream of the reactor followed by a catalytic convertor to avoid discharging carbon monoxide in the environment. Three measurement devices are used in this set-up: a flow controller to measure and control the inlet gas flow rate, an optical emission spectrometer (OES) Avasoft 8 AvaSpec ULS2048-USB2 from Avantes designed to record spectrums between wavelengths 200 and 1100 nm, and a gas chromatographer (GC) GC-2014 SHIMADZU to measure the species in gas products.
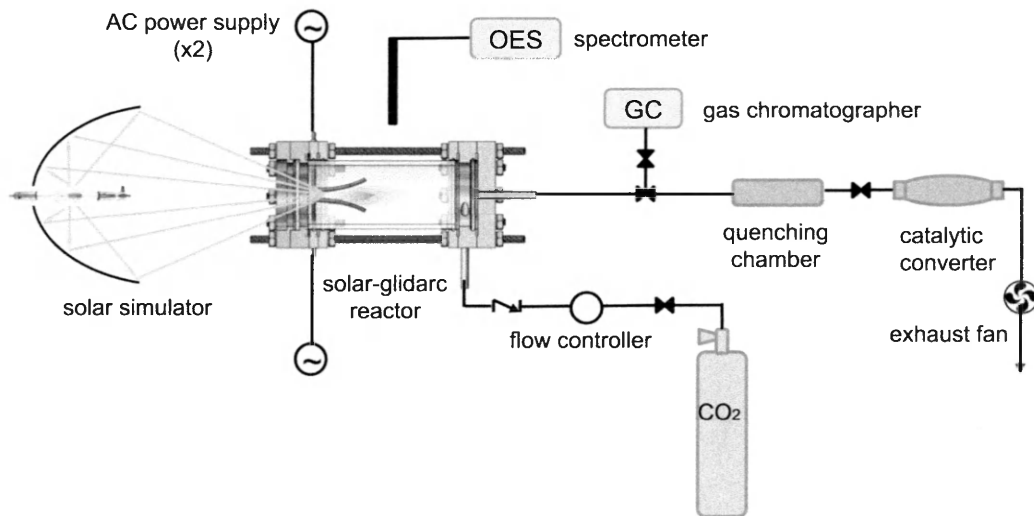
Fig. 4-1: Experimental solar-glidarc system set-up.

The above experimental set-up allows to perform two types of investigations: off-solar (plasma only) characterization tests to evaluate the generation of plasma and its characteristics in both vertical and horizontal orientation, and on-solar (solar-plasma) experimental runs to evaluate the effects of the solar-plasma interaction and the CO_2 chemical decomposition process. These off-solar and on-solar set-ups are depicted in Fig. 4-2.
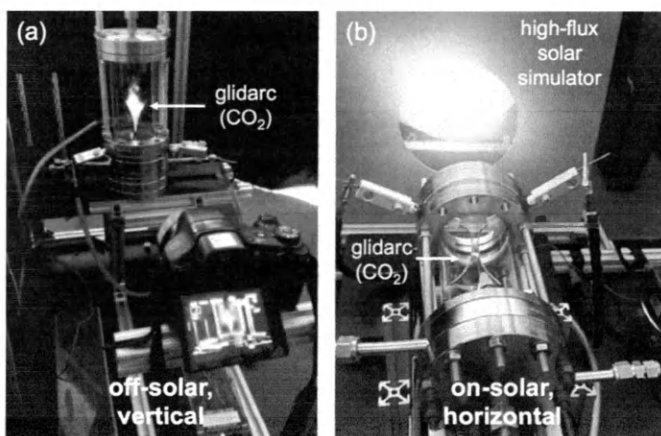
Fig. 4-2: Experimental set-up for solar-glidarc chemical synthesis: (a) off-solar vertical orientation and (b) on-solar horizontal orientation.

4.2. Off-solar plasma characterization

To characterize the plasma, at first, the off-solar (plasma only) tests were performed to analyze the behavior of the plasma inside the reactor chamber. A set of images was taken from the side and top views, using the experimental set-up shown in Fig. 4-2(a). The images were recorded on two characteristic orientations: vertical and horizontal. The vertical orientation is the most favorable in terms of gliding arc dynamics, as the low-density plasma tends to glide naturally due to buoyancy within the high-density feedstock gas. The horizontal orientation is most critical in terms of plasma confinement but depicts the extreme positioning of the reactor if placed within a solar-tracking concentrator.

38

A high-speed camera is used to capture images for arc dynamics analyses such as determination of the arc velocity and its temporal evolution along the electrodes (Fig. 4-3). Figure 4-3 shows that the arc initiates from the lowest point (6 mm gap (d_b) between the 3 electrodes), which corresponds to time t_0; then it evolves upward while remaining attached to the electrodes at 3 points forming a Y-shaped plasma volume until it reaches the top of the electrodes at t_5 where it extinguishes. This analysis allowed estimating an average cycle period of 102 ms for the AXR and 610 ms for the RVX configuration. The longer cycle time in the latter is explained by the swirl flow in one direction, followed by a reverse tornado in the opposite direction, as discussed in Section 2.
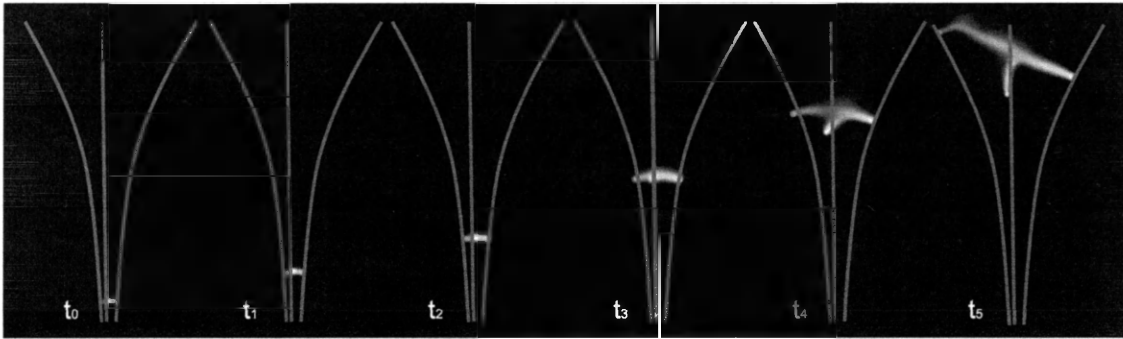
Fig. 4-3: Arc dynamics within the solar-glidarc reactor under no-solar irradiation conditions for the RVX configuration (off-solar, vertical orientation, 15 slpm).

A qualitative analysis is performed to observe the response of the plasma while varying the flow rate. From this analysis, the best cases are obtained and further analyzed, quantitatively, using a Python image processing tool kit to estimate the size of the plasma in terms of its volume. The images for volume quantification are taken using a DSLR camera (long-exposure) to emphasize the volumetric extent of the plasma (Fig.4-4). The results in Fig. 4-4 show that the plasma behaves differently whether the reactor is placed vertically or horizontally for different flow rates. This provides preeminent information on the performance of the two reactor configurations. The results in Fig. 4-4 show that the RVX configuration is more affected by the reactor orientation as compared to the AXR one. In vertical orientation, beyond 4 slpm, both RVX and AXR reactors generate a qualitatively similar plasma plume. Whereas, at lower flow rates and

horizontal orientation, the plasma volume in the RVX reactor is significantly shortened compared to that for the AXR one. At higher flow rates, above 8 slpm, the AXR plasma volume becomes insensitive to the reactor orientation, while the RVX plasma volume starts to expand, but remains significantly lower than the AXR one.
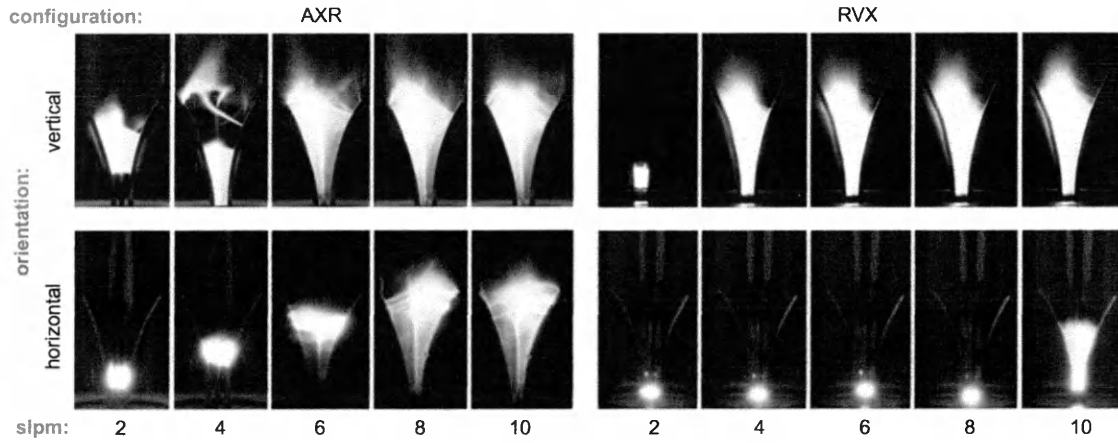
Fig. 4-4: Plasma formation under different reactor orientations: long-exposure optical images of the plasma for the axi-radial (AXR) and reverse-vortex (RVX) configurations for vertical and horizontal orientations and for different flow rates (2 to 10 slpm).

An optical ray-tracing simulation performed previously confirmed that the bigger the plasma volume, the better the interaction solar-plasma when assuming the plasma as an absorbing medium. Based on this observation, the volume of plasma generated for each test condition (flow rate and orientation) is estimated. The estimation of the plasma volume is not trivial due to its irregularities and dynamics (continuous motion and oscillations). To simplify the calculation, the plasma volume is approximated with a prismatic shape, as depicted in Fig. 4-5 (a). Using this approximation, the plasma volume is estimated using:

$$V = \tfrac{1}{3}h(A_1 + A_b + (A_1 A_b)^{\frac{1}{2}}),$$ (10)

where A_b is the surface at the base of the prism, where the plasma generates; h is the maximum height attained by the plasma before extinction; and A_1 corresponds to the surface obtained by determining the laterally-projected distance of the equilateral triangle

40

$(A_1 = \sqrt{3}L^2/4)$ formed by the 3 electrodes (Fig. 4-5(b)). This length L is estimated using both the image processing and Thales's intercept theorem, $\overline{AB}/\overline{CD} = \overline{SI}/\overline{SK}$, as depicted in Fig. 4-5 (c).
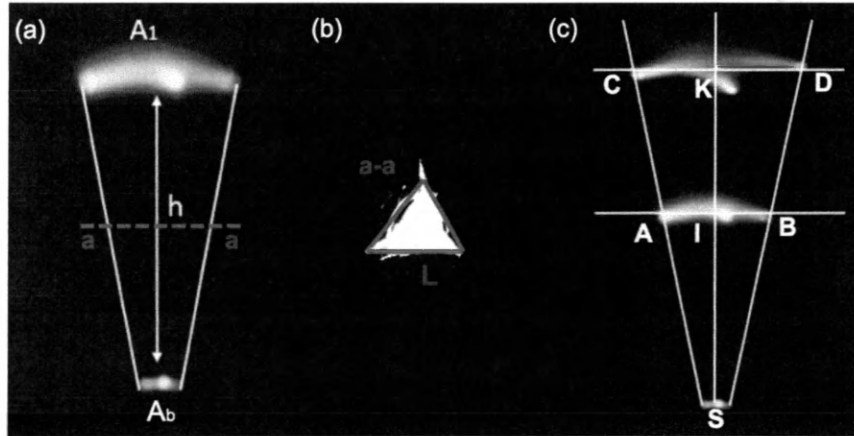
Fig. 4-5: Plasma volume calculation: (a) approximation of the plasma volume as a prism, (b) top view of the plasma volume from a long-exposure image and approximated by an equilateral triangle, and (c) Thales's intercept theorem applied for the estimation of L.
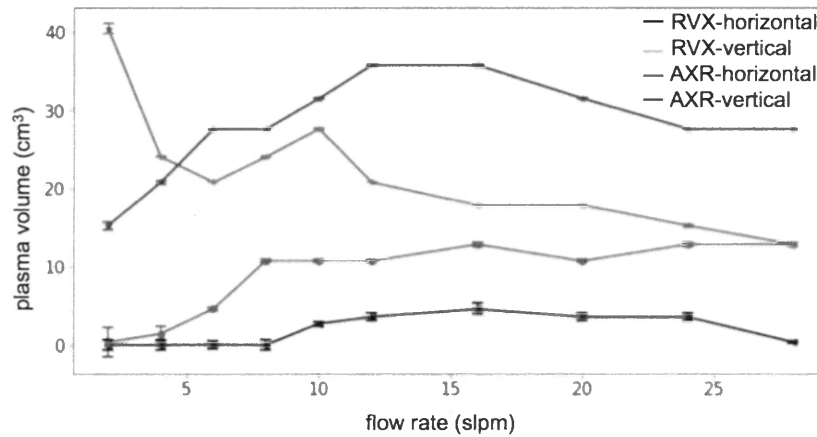
Fig. 4-6: Plasma volume for each reactor configuration and orientation as function of flow rate.

The height between A_l and A_b (top and bottom surfaces) is obtained experimentally. The volume calculated using Eq. (10) is applied to each flow rate condition and plotted in Fig. 6. Figure 6 shows that for both orientations, vertical and horizontal, the axi-radial (AXR) configuration out-performs the reverse-vortex (RVX) one in generating a larger plasma volume. The difference is accentuated in the vertical orientation, while it remains relatively constant for the horizontal orientation for the range of 10 to 24 slpm. Beyond 24 slpm, the RVX plasma plunges while the AXR maintains an almost constant volume. The plasma in the RVX reactor becomes constricted due to the strong vortex inside the cavity.

4.3 Solar-plasma characterization (on-solar)

4.3.1 Spectral absorption

Solar absorption by the plasma was tested at 3 different high-flux solar simulator power levels and one case with low intensity light (200 W incandescent lamp). Regarding the solar simulator, the intensity was adjusted based on varying the amperage: 80, 100, and 120 A, which respectively correspond to 350, 440, and 525 W of radiative power into the reactor chamber. The radiative power from the lamp into the reactor was estimated to $\sim$ 20 W. The plasma power is maintained constant at 240 W for all the experiments.
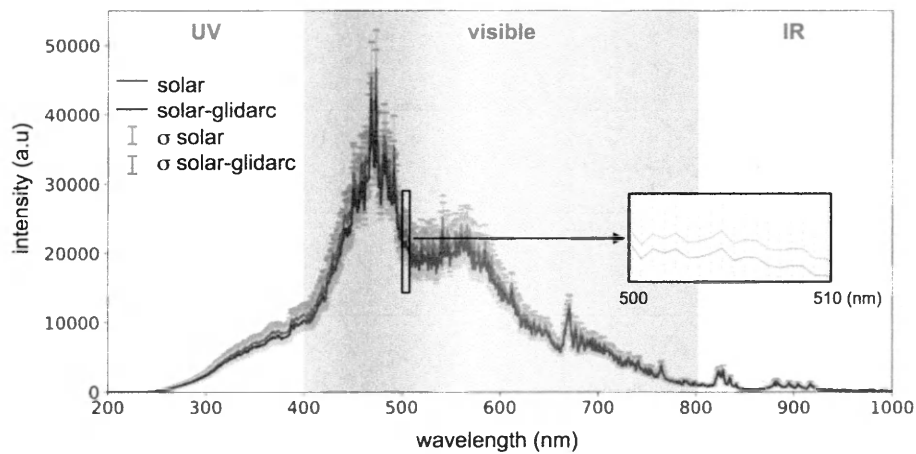
Fig. 4-7: Spectral absorption test results under solar-only and solar-glidarc conditions for 525 W of incident solar radiation and 240 W of electrical energy from the plasma.

To collect absorptance data, the spectrometer was placed at the end of the reactor. In the absence of plasma, the spectrometer, through a fiber-optic probe, reads 100% of the signal emanated from the light-source (characterizing I_0, see Eq. (3)). Then, when the plasma is introduced, the signal is recorded again (providing a measure of I) and compared with the baseline signal previously taken. Figure 4-7 shows representative results of the spectra of the light source (solar) as compared to the one from the combined solar-glidarc over the ultraviolet (UV), visible, and infrared (IR) spectral regions. The continuous-line data indicate temporal-averaged values, whereas the error bars quantify the range of spectral intensity temporal variation. The insert in Fig. 4-7 shows more clearly the difference between the base and plasma-absorbed spectra. The results show wide-range absorption of radiation as the spectrum of the light source (solar) is higher than the solar-glidarc spectrum throughout most of the measured spectral range.

4.3.2 Temporal absorption and arc plasma dynamic

To assert the relation between the temporal evolution of the arc and the net absorption of radiation, spectrum data were collected using the procedure described in Section 3.4.3.1 at different time intervals for the low-level (200 W) radiation source. The dynamics of the arc plasma were captured using the DSLR camera. The temporal spectral data were mapped to the dynamic images of the arc plasma as it goes through its gliding cycle. Figure 8 shows the dynamics of the arc for the AXR configuration as it glides from the ignition point corresponding to t_0 to its maximum elongation at the extinction point at t_3. The temporal net absorption shows that greater absorption is achieved for the larger plasma volume.

A well-known characteristic of gliding arcs is that they originate as so-called thermal discharges, characterized by a state of Local Thermodynamic Equilibrium (LTE) between free electrons and heavy-species (molecules, atoms, ions), and then evolve as non-thermal discharges having a state of non-LTE (NLTE) in which the electrons have significantly higher energy than the heavy-species (Fridman, 2008). The results in Fig. 8

suggest that the plasma is able to absorb significantly more solar radiation while in a nonequilibrium (NLTE) state.
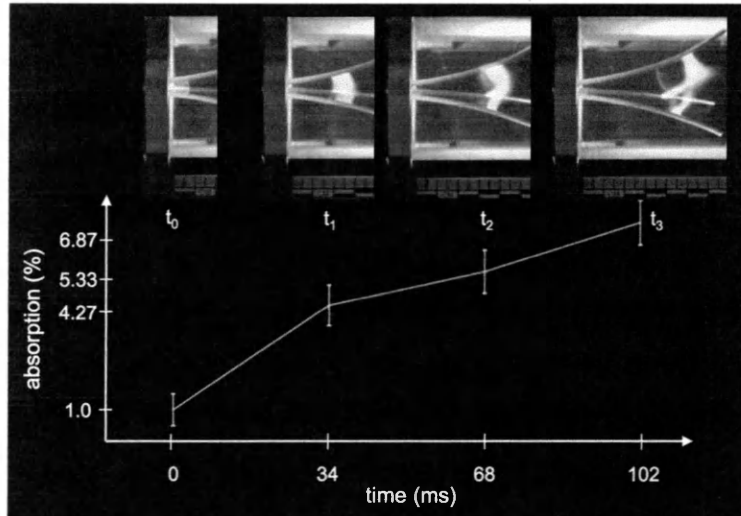
Fig. 4-8: Plasma-arc dynamics and net solar absorption for the AXR solar-glidarc reactor operating with a 200 W light source.

4.3.3 Net radiation absorption

The absorption efficiency given by Eq. (3) was calculated as function of incident solar power for both reactor configurations. Figure 4-9(a) shows a net increase of absorption as the solar-plasma power (P_{psolar} + P_{plasma}) increases from 590 W to 765 W, corresponding to a highest absorption for both reactors. This result suggests that increasing the solar influx increases the absorption of solar radiation by the CO_2 plasma. Although both configurations recorded an increase in absorption, the RVX reactor shows higher absorption as compared to the AXR reactor at 765 W (i.e. 7% for AXR compared to 18% for RVX). Figure 4-9(b) shows a whisker plot of the same data in Fig. 4-9(a) indicating the two medians for the two reactor configurations; a median of 4.68% for the AXR reactor and 9.34 % for the RVX reactor. Therefore, the results in Fig. 4-9(b) depict the improved performance of the RVX over the AXR in terms of radiation absorption efficiency.
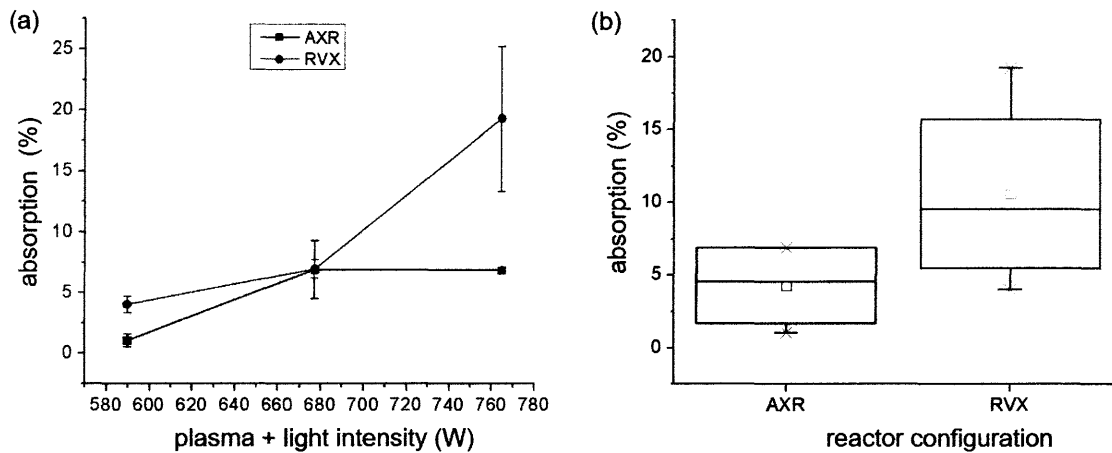
Fig. 4-9: Total absorption test results: (a) absorption at various light source intensities: 350, 440, and 525 W (constant plasma power of 240 W) and (b) net absorption for the AXR and RVX reactor configurations at 10 slpm.

4.4. Preliminary CO_2 dissociation in the solar-gliding arc plasma reactor

A gas chromatographic analysis was performed on the samples collected for the test conditions: plasma only, 200 W light source (20 W into the reactor), 350 and 525 W, and for a flow rate of 10 slpm. The carbon dioxide conversion efficiency was evaluated using Eq. (4). The results in Figure 4-10(a) indicate that the CO_2 conversion efficiency of the AXR reactor outperforms that of the RVX. This result is attributed to a significantly more stable plasma observed at this flow rate in the AXR configuration (as discussed in Section 3.4.2), despite a relatively low residence time (4.10 s). In contrast, the decline of CO_2 conversion for the RVX configuration is explained by a constricted plasma for the same flow rate (10 slpm). In addition, an inflection point observed for both configurations at 590 W is due to a low absorption observed at this test point, as indicated on Fig. 4-10(a) as compared to 680 and 765 W. Figure 4-10(b) shows the energy efficiency per SEI evaluated for off-solar (plasma only) and the combined solar-plasma operation. These results clearly show the dependency of the energy efficiency on the feedstock conversion: increasing light intensity results in higher conversion for the AXR reactor, while the opposite is true for the RVX one. It is important to note that the plasma

45

SEI is estimated at 0.248 eV/molecule for the plasma without solar, and then after, for plasma coupled with solar at various light intensities (350, 440, and 525 W), as shown on Fig. 4-10(b). The plasma energy efficiency shown for the RVX configuration (Fig. 4-10(b)) is comparable to that reported by Nunnally and collaborators using a reverse-vortex flow Glidarc reactor achieving efficiencies in the range of 18-43% for flow rate in the range of 14 to 40 slpm (Nunnally et al., 2011). This result indicates the marked advantage of the solar radiation influx on increasing CO_2 decomposition in an otherwise plasma-only process.
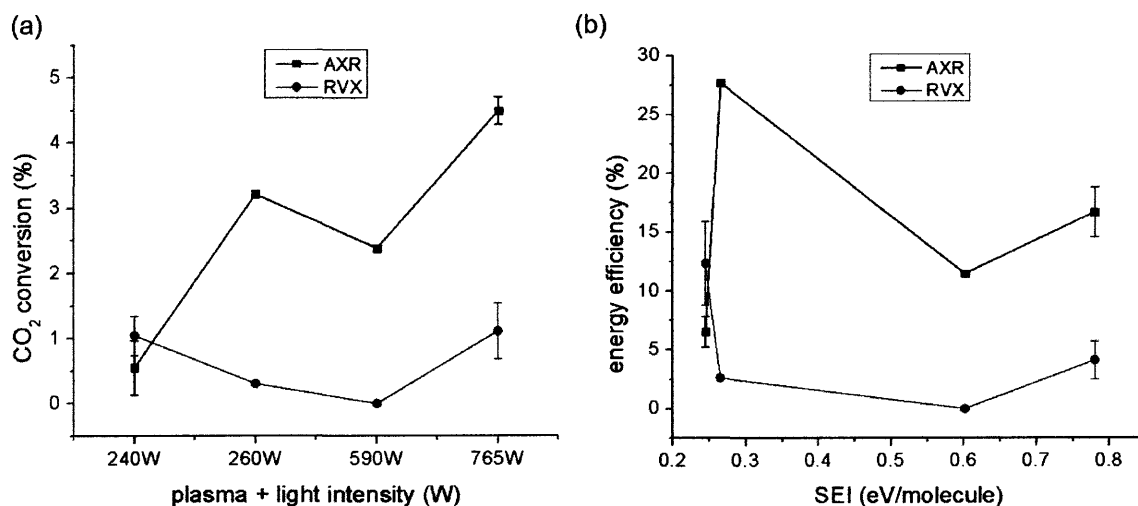
Fig. 4-10: Solar-plasma reactor performance: (a) CO_2 conversion and (b) energy efficiency versus specific energy input (SEI) for the AXR and RVX configurations at 10 slpm.

It is has been established the solar-gliding arc plasma reactor is capable of chemical processing gas phase carbon dioxide. The results presented above are obtained based on a randomly selected flow rate of 10 slpm. The results indicate that the 2 reactor configurations perform differently which requires a further detailed investigation on the effectiveness at various operating conditions.

Chapter 5 Solar-glidarc reactor operation and performance assessment

5.1. Design of Experiment methodology

The research focuses on the determination, following a Design Of Experiments (DOE) procedure, of optimal process configurations for the processing of CO_2, CH_4, and H_2O mixtures using the developed solar-glidarc reactor. The DOE is based on a multi-level, multi-factors approach (Taguchi, 1987). DOE is a structured approach to experimentation that provides a means to determine target operational characteristics, such as maximum efficiency, from a limited set of experimental data. The DOE Taguchi approach, which uses a set of balanced orthogonal arrays to generate and perform statistical analysis based on the signal-to-noise ratio (ratio of the measured mean to its standard deviation), will be used in the planned experiments. This method is commonly used in solving optimization problems in engineering (Box, Hunter & Hunter, 1978).

Table 1: Main factors and their respective settings (levels).

	Flow rate	Solar	Plasma	Reactor
Level-1	1. 5 slpm	1. 0 A	1. No	1. RVX
Level-2	2. 10 slpm	2. 2.45 W	2. Yes	2. AXR
Level-3	3. 15 slpm	3. 80 A		
Level-4	4. 20 slpm	4. 100 A		
Level-5		5. 120 A		
Level-6		6. 140 A		

First, four factors with high potential impact on the process were considered: (1) flow rate in a range 5 – 20 slpm, (2) solar power input in the range 0 – 600 W, (3) plasma versus no-plasma operation, (4) reactor configuration, i.e. AXR or RVX. These factors

and the values used to probe their respective ranges are shown in Table 1. For these 4 factors, assuming a two-level orthogonal array would requires 2^5 or 32 experiment (96 for a mixed-level proposed); this type of orthogonal array is labeled L_{32} and is constituted by 32 rows, one per set of experimental conditions. While 32 experimental runs are required in a full factorial design of a L_{32}, a fractional factorial (L_{16}) was used to reduce the runs by half (16 runs). Table 1 shows the factors and their respective settings (levels).

Table 2 shows the scheme used to convert a 2-level base DOE to a multi-level DOE (Taguchi, 1987; Montgomery, 2012). Figure 5-1 shows a linear graph adopted to study the possible interactions between the 5 factors. The DOE is used to evaluate the solar-plasma reactor performance for 3 chemical processes: the dissociation of CO_2, the processing of $CO_2 - H_2O$ mixtures, and the processing of $CO_2 - CH_4$ mixtures.

Table 2: Scheme to generate multi-level factors by taking a 2-level factor, such as A, B or C, and mixing them to obtain a higher-level factor, such X and Y.

A (2 level)	B (2 level)	X (4 level)
1	1	1
1	2	2
2	1	3
2	2	4

A (2 level)	B (2 level)	C (2 level)	Y (8 level)
1	1	1	1
1	1	2	2
1	2	1	3
1	2	2	4
2	1	1	5
2	1	2	6
2	2	1	7
2	2	2	8
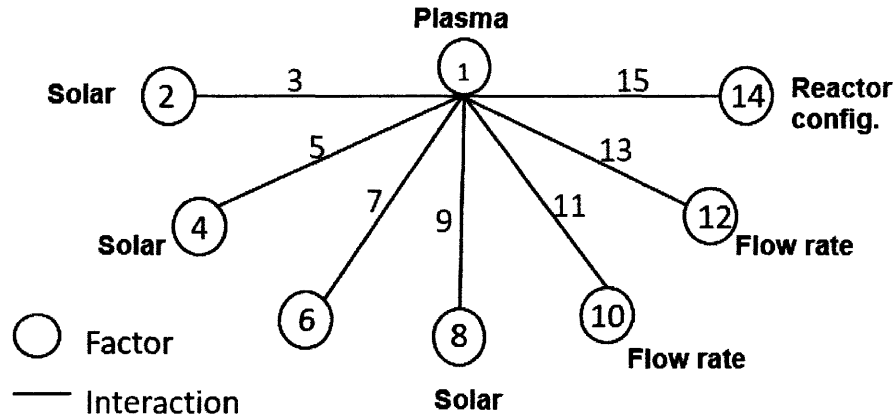
Fig. 5-1: Linear graph for the 4 factors and their interactions: standard 2-level (L_{16}). The numbers in the circles indicate main-factors, while colored numbers on the bars represent the interaction between two main factors.
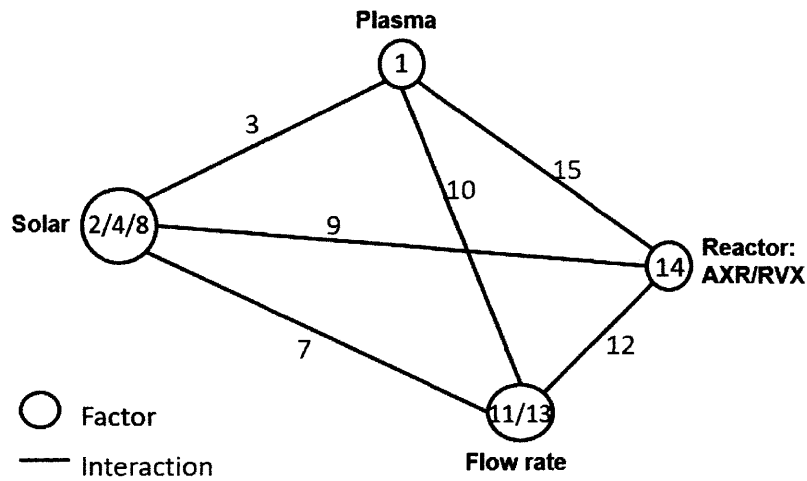
Fig. 5-2: Modified standard 2-level linear graph to a multi-level 4 factors analysis and their interactions: (L_{16}). Numbers in the circles indicate main-factors, while colored numbers on the bar shows the interaction between two main factors.

Figure 5-2 shows the modified linear graph that considers the mixed multi-levels of the four factors. The obtained linear graph is important to study the interactions between the main factors, as it will be presented in the subsequent sections.

Data are collected following the matrix format presented in Fig. 5-3. In this matrix, 16 experiments are run in various combinations of the 4 selected factors. For this work, three responses are measured: Response1 is the conversion of the reacting gases, Response2 is the gas temperature, and Response3 three the electrode weight loss or gain.

Factors/Interactions

1	2	3	4	5	6	7DE	8	9	10	11CE	12	13BE	14AE	15		Response1	Response2	Response3
A	B	AB	C	AC	BC	ABC	D	AD	BD	ABD	CD	ACD	BDC	ABCD				
1	1	1	1	1	1	1	1	1	1	1	1	1	1	1		-	-	-
1	1	1	1	1	1	1	2	2	2	2	2	2	2	2		-	-	-
1	1	1	2	2	2	2	1	1	1	2	2	2	2	2		-		-
1	1	1	2	2	2	2	2	2	2	2	1	1	1	1		-		-
1	2	2	1	1	2	2	1	1	2	2	1	1	2	2		-		-
1	2	2	1	1	2	2	2	2	1	1	2	2	1	1		-		-
1	2	2	2	2	1	1	1	1	2	2	2	2	1	1	=	-		-
1	2	2	2	2	1	1	2	2	1	1	1	1	2	2		-		-
2	1	2	1	2	1	2	1	2	1	2	1	2	1	2		-		-
2	1	2	1	2	1	2	2	1	2	1	2	1	2	1		-		-
2	1	2	2	1	2	1	1	2	1	2	2	1	2	1		-		-
2	1	2	2	1	2	1	2	1	2	1	1	2	1	2		-		-
2	2	1	1	2	2	1	1	2	2	1	1	2	2	1		-		-
2	2	1	1	2	2	1	2	1	1	2	2	1	1	2		-		-
2	2	1	2	1	1	2	1	1	1	1	2	1	1	2		-		-
2	2	1	2	1	1	2	2	2	2	1	2	2	2	1		-		-

Runs (experiments)

Fig. 5-3: Matrix (L16) used to collect 16 experimental runs against 3 set of responses.

5.2. DOE results – phase 1: reactor design optimization using pure CO2

In this section, the DOE results obtained from the initial L16 matrix are presented with respected to the three responses, namely conversion efficiency, gas-product temperature, and electrode erosion. This preliminary step in the DOE analysis is to identify the most significant factors and settings that will lead to higher solar-gliding arc reactor performance. Data are input to the software MINITAB 18 for statistical analyses.

5.2.1. Carbon dioxide conversion

Phase one of the DOE results correspond to the case of pure CO_2 dissociation in the solar-gliding arc reactor. Figure 5-4 shows the results of CO_2 conversion from the 16 runs; the results indicate a maximum conversion of 4.2% obtained at run number 15. The results also show significant conversion when solar interacts with plasma as compared to purely solar runs.
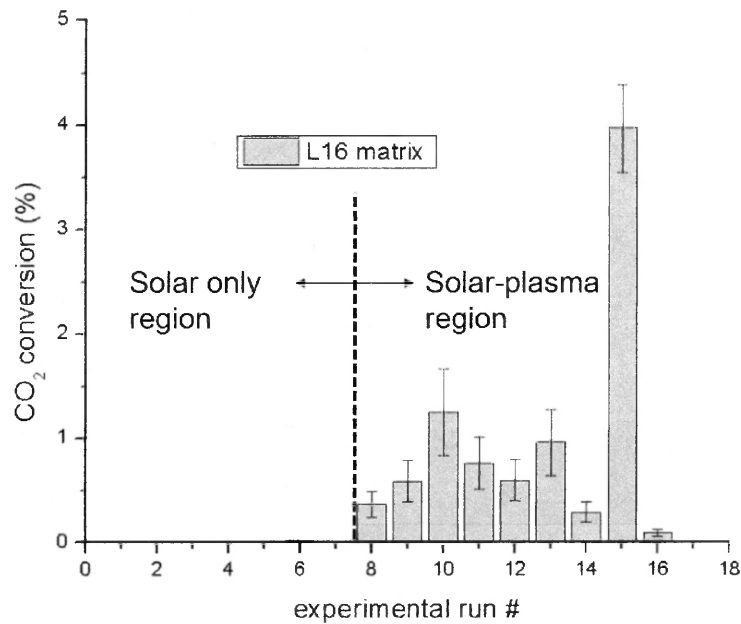
Fig. 5-4: Matrix (L_{16}) – conversion results of the 16 experimental runs.

The results presented in Fig. 5-4 provide the conversion per run but does not provide information on which factors and settings (levels) are significant. The DOE analysis of the means presented in Fig. 5-5 points out the important factors with the settings capable of leveraging the overall conversion for optimization purposes. It can be inferred from Fig. 5-5 that the following factors are significant: solar, plasma, and flow rate. Although less significant than the first 3, the reactor configuration indicates that operating the solar-gliding arc reactor in AXR mode is more beneficial in terms of conversion than the RVX, confirming the preliminary results presented in Section 4.4.

To complement the analysis, the interactions between the four main factors are plotted in Fig. 5-6. The latter summarizes the interactions in form of a matrix, which outlines the significant interactions and their respective settings. Plasma shows strong interaction with solar at setting 2, with flow and reactor configuration both at setting 1. In addition to its strong interaction with plasma, solar does indicate a notable interaction with flow and reactor configuration, both at setting 1.
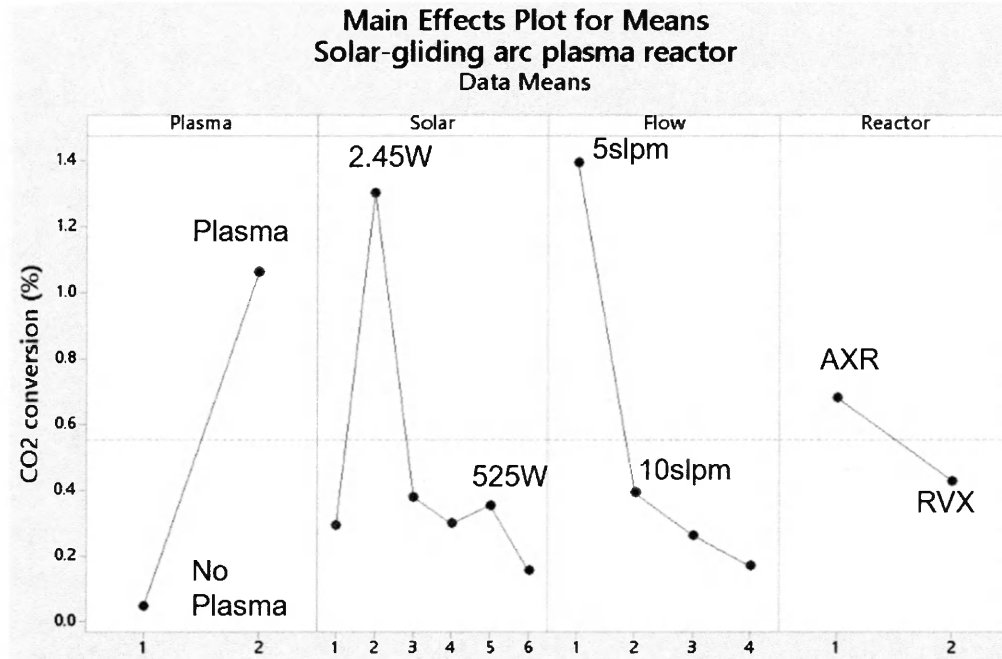
Fig. 5-5: Matrix (L_{16}) – Main effects plot based on DOE mean analysis indicating significance of factors and their respective settings.
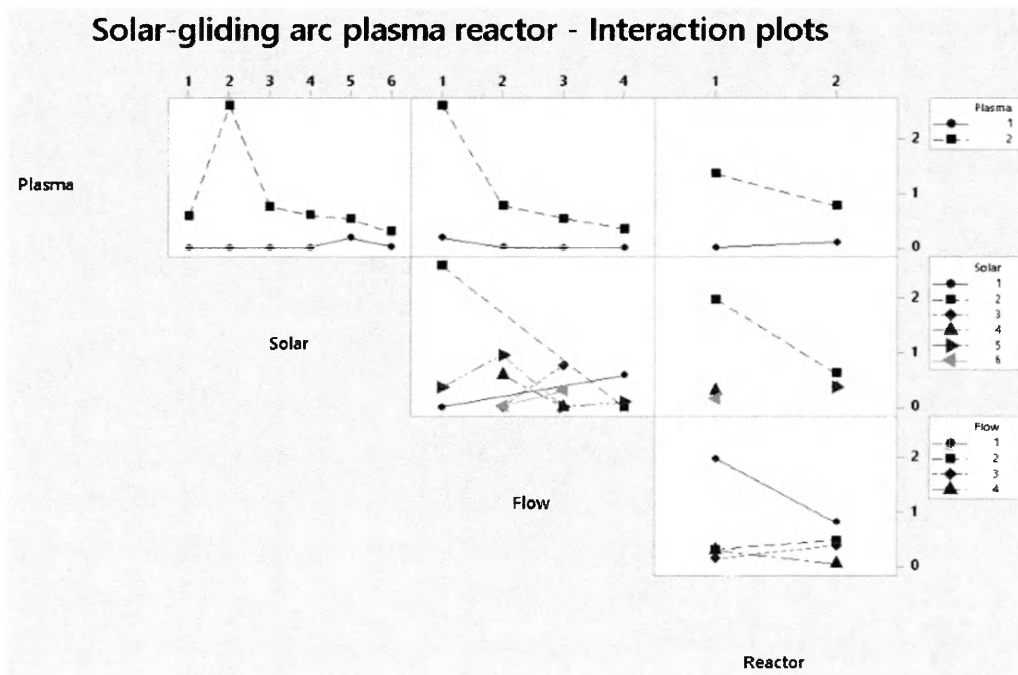
Fig. 5-6: Matrix (L_{16}) – Interaction plots showing the significance of levels.

In summary, the results presented above suggest that operating the solar-plasma reactor at the settings plasma 2, solar 2, flow 1, and reactor 1 should yield higher conversion efficiency. These conditions will be tested in the subsequent sections.

5.2.2 Gas-product temperature

Outflow gas temperature data were collected and analyzed following the same approach as in section 5.2.1. The results are summarized and presented in Fig. 7. Solar and flow rate appears as significant factors in terms of gas temperature. The reactor will operate at higher temperature for settings 4, 5 and 6, which correspond to higher solar flux from the simulator. Flow rate settings 1 and 4 seem to indicate lower gas product temperature as well.

The results suggest that operating with a low intensity light source in the AXR flow configuration at flow rates 5 slpm or 20 slpm will significantly lower the operating temperature of the process.
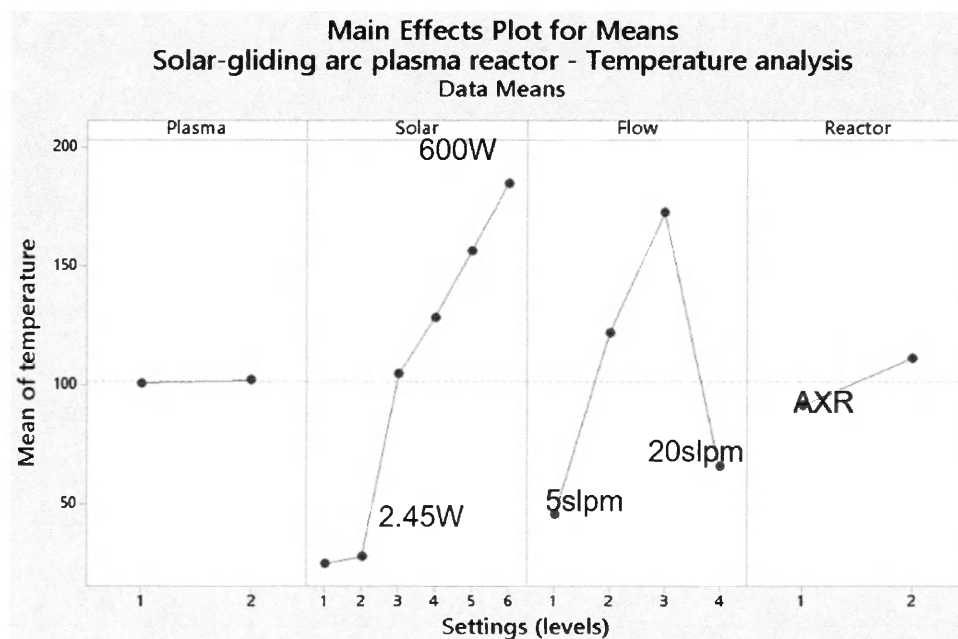
Fig. 5-7: Matrix (L_{16}) – Temperature plots showing significant factors and settings.

5.2.3 Electrode erosion

The measure of weight loss or gain by an electrode is to account for surface chemical deposition during the solar-plasma chemical process, i.e. a film deposition of solid compound will result in gain of weight or an interaction between copper electrode and plasma species resulting in consumption of copper results in weight loss. To measure the weight loss or gain, the weight of each electrode is measured before and after each experiment. To avoid bias in the measurement, each run is operated with a new set of electrodes (3 per set). The electrode erosion is evaluated using:

$$erosion = \frac{m_{in} - m_{out}}{m_{in}} \times 100(\%),$$ (11)

where m_{in} and m_{out} are, respectively, the mass before and after the experiment. The DOE results presented in Fig. 8 indicate that plasma and solar play a significant role in the erosion of the electrodes. Further analyses performed on a segregated data per reactor type and flow, both in the presence of plasma or solar reveal the effects of increasing solar increases the erosion (Fig. 8 (a) for AXR and Fig. 8 (b) for RVX).
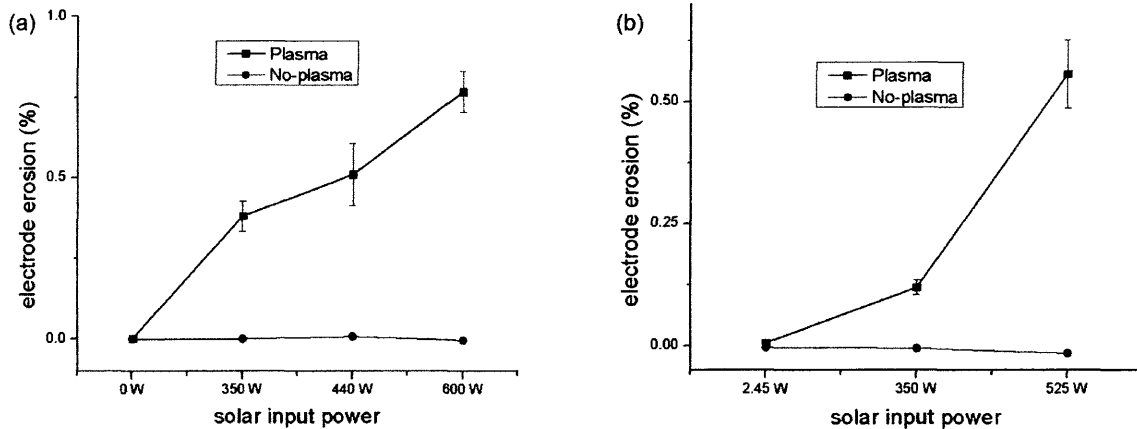
Fig. 5-8: Net effect of plasma and solar on electrode erosion: (a) AXR, (b) RVX.

54

5.2.4 DOE summary

The first phase of experiments involved 16 runs evaluated with respect to pure CO_2 conversion, gas-product temperature, and electrode erosion. The structured DOE results summarized in Table 3 are used as guidance for the next set of experiment with a restricted number of factors following the first round of 16 experiments.

Table 3: Summary of optimal experimental conditions determined from L_{16} matrix runs.

Outcome	Plasma	Solar	Flow	Reactor
Conversion	Significant	Significant	Significant	
(Highest the better)	2 (include)	2 (2.45W)	1 (5slpm)	2 (AXR)
Gas Temp		Significant		
(Lowest the better)		2 (2.45W)		
Erosion	Significant	Significant		
(Lowest the better)	1*	2 (2.45W)		1 (RVX)

Based on the results in Table 3, the following parameters are selected for the next phase of the experiment: the AXR rector configuration is preferred than the RVX; two flow rates, namely, 5 and 10 slpm are retained; and two solar settings, 2.45 W and 525 W, to enable the investigation of both low and high intensity light source.

5.3. DOE results – phase 2: reactor design optimization using gas mixtures

5.3.1 DOE L_8 matrix approach

The results presented in Section 4.1 indicate that the most significant factors are the solar flux and the use (or not) of plasma. The first spans the range of solar intensity from setting the solar simulator to operate at 120 A (525 W into the reactor) to using the 200 W incandescent lamp (2.45 W into the reactor as radiative power). The third and fourth significant factors are the reactor configuration and the flow rate. Although the reactor configuration is not as significant as the first three factors (solar intensity, plasma,

and flow rate), the results suggest running the process with a solar-glidarc in AXR mode is predicted to yield higher efficiencies. The next step in the optimization process focuses on operating the solar-glidarc reactor at the experimental conditions determined above and summarized in Table 4 below.

Table 4: Optimal experimental conditions for second round of experiment – L_8 matrix.

	Flow rate	Solar	Plasma	Reactor	CO_2/CH_4	Pure CO_2	CO_2/H_2O
Level-1	5slpm	525 W	Maximum	AXR	4/1	-	saturated
Level-2	10slpm	2.45 W	-	RVX	-	-	saturated

The list of factors and settings in Table 4 translate into a significant reduction of the number of experiments to run, as it focuses on 2-level factors only, as compared to the multi-level factors in the initial design (Table 1). The factors specified in Table 4 could be handled with a resolution level of 4 in a L_8 DOE approach, which requires only 8 experiments. The 4 factors include the flow rate, solar input, and two mixture-ratios CO_2/CH_4 (in a ratio 4/1) and CO_2/H_2O (saturated CO_2 with water vapor). The ration of CO_2/CH_4 has been chosen following Bogaerts et al., 2016, with a target corresponding to attaining maximum yield of hydrogen (H_2) and carbon monoxide (CO). For reference, yields of 34% for H_2 and 10% for CO were reported in Bogaerts et al., 2016 using plasma-only processes (based on dielectric barrier discharge and microwave discharges). Similar ratios were used by Liu and collaborators (Liu et al., 2016) using an AC-pulsed gliding arc plasma reactor, achieving 29% and 22% conversion of CH_4 and CO_2, respectively.

5.3.2 Optimized operating parameters using DOE L_8 matrix

The second set of experiments consisted of 8 runs repeated two times. The main factors considered are solar on two levels (low light source – 2.45 W and high intensity light source – 525 W), flow rate on two level (5 slpm and 10 slpm), reactor configuration on two level (AXR and RVX), and gas mixture ration on two levels (CO_2/CH_4) the

results obtained for conversion efficiency with the reduced 8 runs are presented in Fig. 5-9. The larger the span (length of the segment), the more significant is the factor. Based on this criterion, reactor configuration is the most significant factor followed by flow rate and solar input. To predict the highest conversion, the best combination is to operate the solar-gliding arc reactor in an AXR configuration at 5 slpm with the low intensity light source (2.45 W).

From the results presented in Fig. 5-9, the final combination of settings with potential to achieve higher chemical processing conversion are kept constant: AXR reactor configuration and lower flow rate equal to 5 slpm. The runs are performed by changing the solar input-flux for the two cases of reacting gas ratio: CO_2/CH_4 and CO_2/H_2O.

Main Effects Plot for Means
Solar-gliding arc plasma reactor - L8 conversion analysis
Data Means
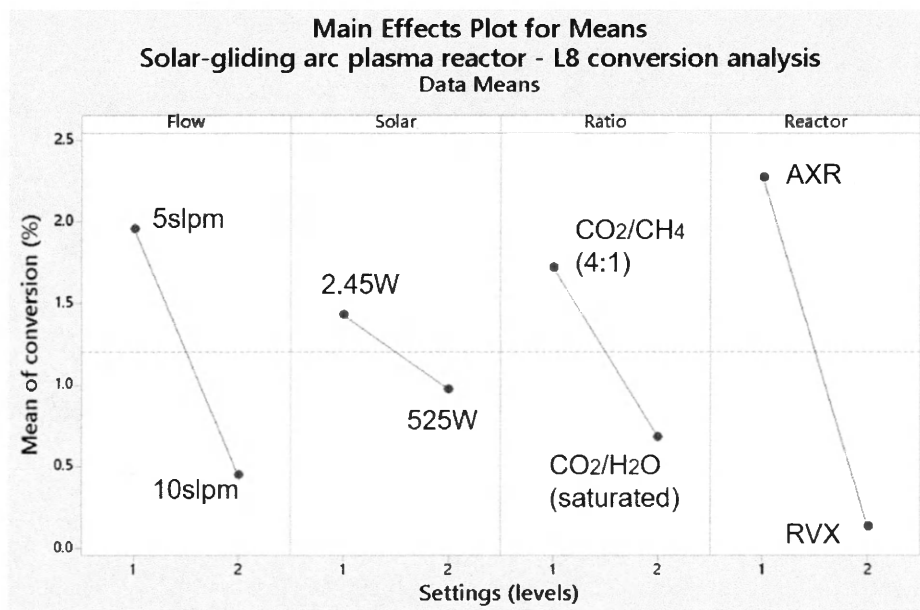
Fig. 5-9: Matrix (L_8) – Main effects plot based on DOE mean analysis indicating significance of factors and their respective settings.

5.4. Conversion and energy efficiencies for pure CO_2 decomposition

The optimal operating conditions of the solar-gliding arc plasma have been set in Section 5.2.2. The solar-glidarc reactor was run at these conditions between 30 to 35

minutes. The experiment was repeated 2 to 3 times to evaluate the variability of data (quantified by error bars). Sample of gas products are collected and analyzed in a gas chromatographer for composition species along with their quantity present in the gas mixture. The conversion efficiency is calculated based on equation (1), which is then used in the estimation of the energy efficiency obtained from equation (3). The solar flux inputs considered in the case of pure CO_2 dissociation are: 0 W (plasma only, no solar), 2.45 W (low intensity light source – incandescent lamp), 350 and 525 W as high intensity light source from the solar simulator. The results presented in Fig. 5-(10(a)) show that for pure CO_2 dissociation, the maximum conversion is attained when using low intensity light source.
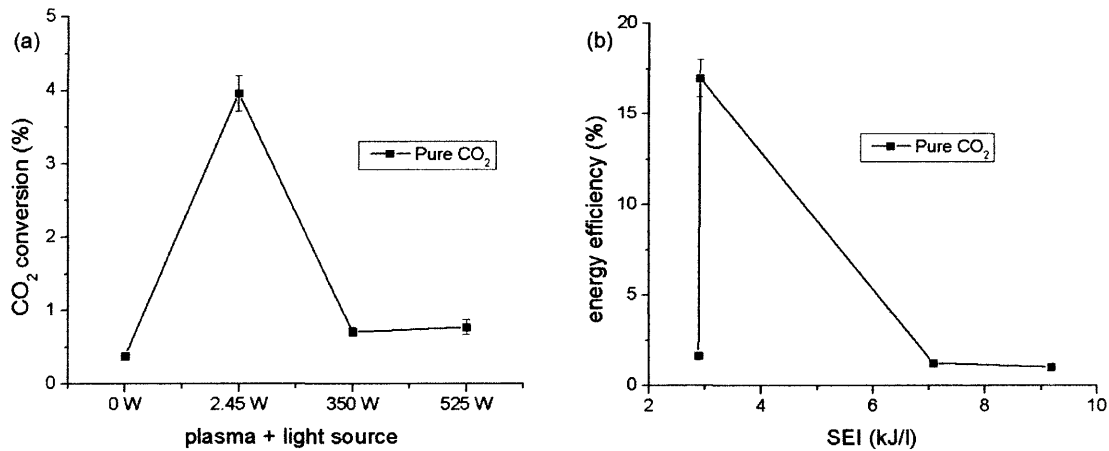
Fig. 5-10: Processing of pure CO_2: (a) conversion of CO_2 in AXR at 5 slpm flow rate, (b) energy efficiency.

5.5. Conversion and energy efficiencies for CO_2-CH_4 processing

From the previous results which show the significance of low intensity light source, two more data points were added for the case presented here (reforming of CH_4): low intensity light source at 0.735 and 3.675 W to evaluate the immediate conversion in the vicinity of the existing incandescent lamp (2.45 W). Figure 5-11 shows both the conversion and energy efficiency of the CO_2 reforming of CH_4 in the solar-plasma

gliding arc reactor. The results show an increase in conversion for the two solar intensity settings: 2.45W and 350W. The highest energy efficiency of 22.3% recorded corresponds to the 2.45W condition, and is due to a relatively low specific energy input (SEI).

Although the results indicate a downward energy efficiency trend as the solar power increases, higher conversion of CO_2 is achieved in this combination ($\sim$ 5.7%) compared to that attained for pure CO_2 and CO_2-H_2O.
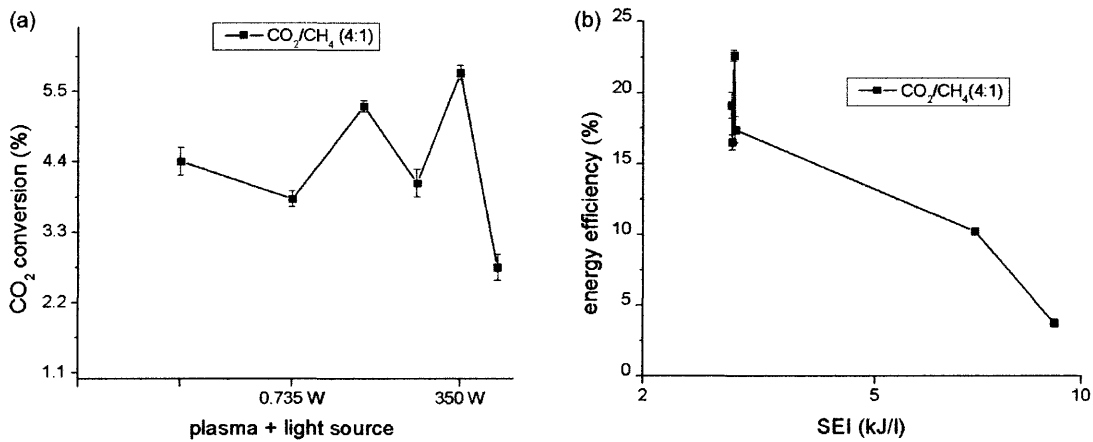
Fig. 5-11: Processing of CO_2-CH_4: (a) conversion of CO_2 in AXR at 5slpm flow rate, (b) energy efficiency.

5.6. Conversion and energy efficiencies for CO_2-H_2O processing

The synthesis of CO_2 and water vapor is realized in the experimental set-up by using water bubbler that ensures the resulting CO_2 stream to be in water vapor-saturated state. Samples are collected and analyzed following the same procedure described in Section 5.3. Figure 5-12 shows the conversion efficiency and the energy efficiency of the CO_2-H_2O conversion process. For this process, high intensity light sources are required to drive both conversion and energy efficiency upward. This behavior is attributed to the presence of water, which absorbs the thermal energy released by both plasma and solar inside the reactor chamber.
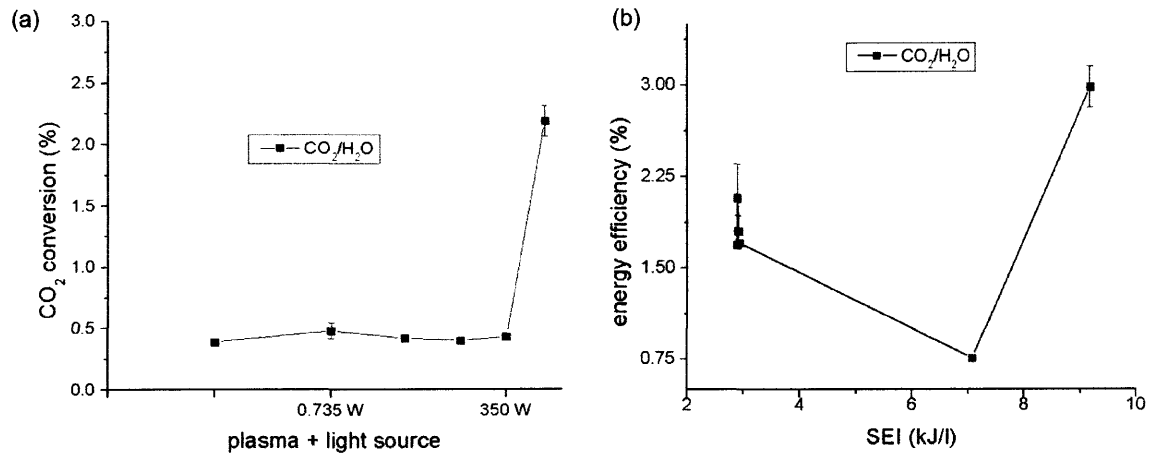
Fig. 5-12: Processing of CO_2-H_2O: (a) conversion of CO_2 in AXR at 5 slpm flow rate, (b) energy efficiency.

Chapter 6 Discussion

6.1. Solar-plasma interaction: photo excitation of gliding arc plasma

The results in this work indicate that plasma does absorb solar photons, as shown in Section 4.3.1. However, the chemical conversion of CO_2 as presented in Sections 5.4 to 5.6 does not follow the net absorption increase behavior with increasing solar input power (Fig. 5-10, Fig. 12). To understand this characteristic of the solar-glidarc chemical conversion process, deeper understanding of the kinetics involved in CO_2 plasma chemical dissociation is required. Fridman et al. (2008) have investigated the different modes of energy transfer in noequilibrium CO_2 plasma. They concluded that he most effective way of energy transfer for CO_2 decomposition is electron transfer through vibrational excitation via: $CO_2^*\left(^1\Sigma^+\right) \rightarrow CO\left(^1\Sigma^+\right) + O\left(^1D\right)$, where $(^1\Sigma^+)$ signifies ground electronic state vibrational level, whereas (^1D) means the ground electronic state. Should the energy be absorbed in a different way, i.e. rotational or electronic excitation of the molecules or atoms, such energy is likely to lead to heating only. The gliding arc plasma is largely acknowledged to favor the vibrational mode of energy transfer. The question remains why does the interaction in high solar input power contribute to the de-activation of the vibrationally excited molecules in the gliding arc plasma? This phenomenon is observed in the experimental results summarized in Fig. 6-1.

61

(a)

(b)

Plasma, no light,
AXR, 20 slpm

Plasma, 2.45 W,
AXR, 20 slpm

(c)

Plasma, 525 W,
AXR, 15 slpm
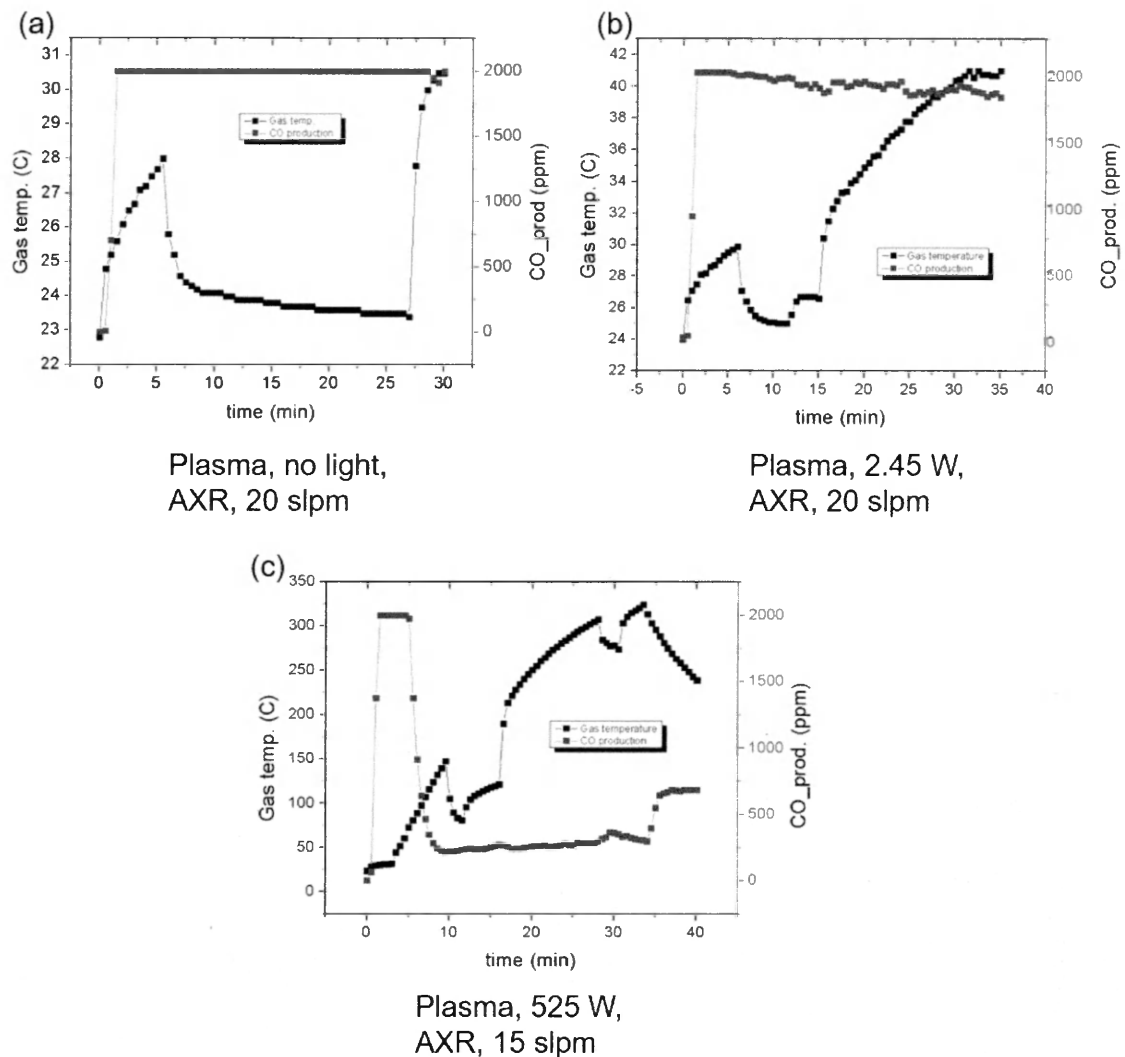
Fig. 6-1: Reduction in production of CO as the solar input power increases. (a) pure plasma, (b) plasma + 2.45 W, (c) plasma + 525 W

Figure 6-1(a) shows the production of carbon monoxide (CO) without solar energy input. A slight decrease in CO production can be observed in Fig. 6-1(b), whereas a significant decrease is observed in Fig. 6-1(c) for a higher solar input power of 525 W. Such behavior may be potentially understood in terms of decrease in activation energy. Transition state theory (TST) states that for a reactant to undergo a chemical transformation to become a product, it has to first be transformed into an activated complex containing the energy necessary to break the inner bond in the process of becoming a new chemical compound (Froment et al., 2011). Therefore, the formation of activated complex population is important to enhance the chemical reaction process (here

62

the formation of vibrationally excited species). To overcome the activation barrier, one needs to produce more excited species to lower the activation energy, i.e.

$$E_a = \Delta H_R + (1 - \Delta n)T ,$$ (12)

where E_a is the activation energy, ΔH_R is the enthalpy of the reaction, Δn is the population of activation complex, and T is the temperature of species. The high CO_2 conversion recorded for the case of low intensity light source (2.45 W) promotes the population of vibrationally excited species in the plasma while the high intensity light source (525 W), although it significantly increases the thermal energy of the gas as sensible heat, as indicated by Fig.6-1 (c), does not promote the population of vibrationally excited species.

6.2. Electrode erosion in solar-gliding arc plasma reactor

Electrode erosion in arc discharges is of primary importance due its relevance in process reproducibility and lifetime (Fridman & Kennedy, 2011). The emission of electrons from the surface of electrode in thermal plasmas occurs via thermionic emission while in non-thermal plasmas due to field emission. In addition, the bombardment of the surface of the electrode by ions and other excited species can lead to secondary emission. Erosion in the solar-glidarc reactor can potentially be caused by the three mechanisms: thermionic due to the high heat flux from the solar simulator, field emission due to the high voltage of the power supplies (20 kV), and secondary electron emission promoted by the AC nature of the driving voltage.
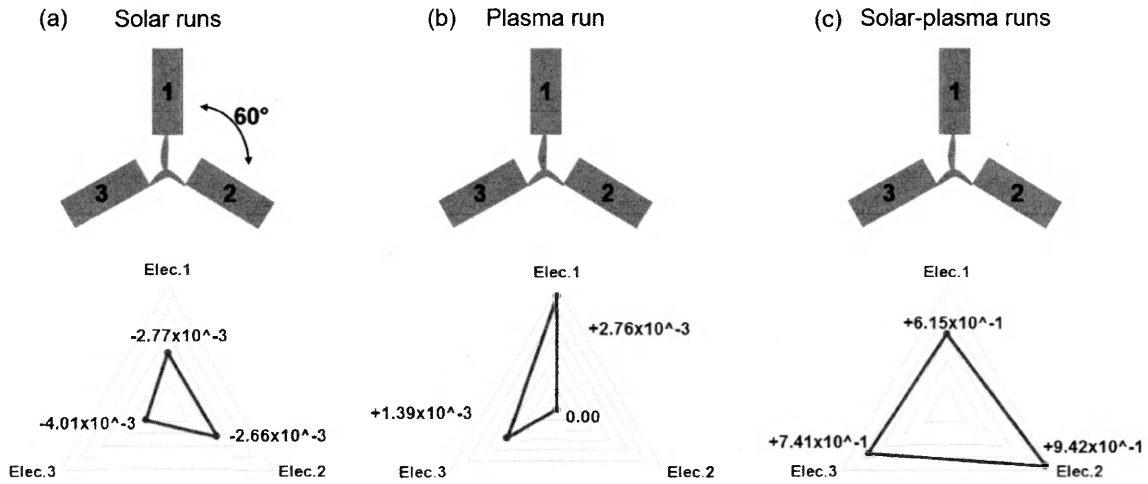
Fig. 6-2: Electrode erosion in solar-glidarc plasma.

Experimental erosion data for the solar-glidarc reactor is summarized in Fig. 6-2. Figure 6-2 (a) shows negative values of erosion, indicating no loss of electrode mass and instead material deposition over the electrode surface, while Fig. 6-2 (b) and (c) display a notable erosion loss when solar and plasma are combined. It can be noted that the erosion is not symmetric across all three electrodes.

Chapter 7 Summary and conclusions

7.1. Summary

The decomposition of carbon dioxide (CO_2) using concentrated solar energy and renewable electricity can help fulfill the increasing need for fuels and chemicals while mitigating environmental emissions. In that regard, the proposed research aims to evaluate the combined use of concentrated solar energy and the nonequilibrium plasma to enhance the efficiency and resiliency of solar thermochemical synthesis processes.

As preliminary work, the characterization of high-flux solar simulator has been completed. This work determined that the simulator delivers a simulated solar radiation flux of 270 Wm^{-2} at the focal point with radiation spectrum that closely resembles that of natural sunlight. Additionally, the design and characterization of a direct solar receiver-reactor fitted with a gliding arc (glidarc) electrical discharge for potentially greater efficiency and continuous operation solar thermochemical synthesis has been presented. The nonequilibrium plasma inside the reactor chamber leads to increased solar energy absorption by the gas-phase atmospheric pressure CO_2 feedstock, potentially enhancing process efficiency; whereas the reliance on electrical energy to sustain the plasma allows compensating for fluctuations in the solar radiation input. Although a catalytic medium can drastically enhance the performance of solar thermochemical reactors, no catalytic component is included in the presented reactors to isolate the role of the plasma on the solar energy - gaseous feedstock interaction. Two solar-glidarc reactor configurations have been investigated: axi-radial (AXR) and reverse-vortex (RVX) flow. The former provides greater control of residence time but presents limited solar-plasma interaction; whereas the latter allows for greater interaction, but requires higher flow rates to confine the plasma, lowering the residence time. The two reactors were constructed and evaluated through three performance indicators: (i) the absorption efficiency of solar radiation by

65

the nonequilibrium atmospheric pressure CO_2 plasma, (ii) the efficiency of conversion (dissociation) of the CO_2 feedstock, and (iii) the energy efficiency of the CO_2 decomposition process. Experimental results established that the interaction between solar radiation and nonequilibrium plasma leads to increased absorption of solar radiation, with median absorption efficiencies of 4.7% and 9.3% for the AXR and RVX configurations, respectively. The maximum CO_2 decomposition obtained was 4.5% for the AXR reactor configuration, significantly greater than the 1% for the RVX one mainly due to a more stable plasma for the same flow rate. A maximum energy efficiency of 25% was achieved by the AXR configuration operating at 10 slpm and low values of specific energy input. The results indicate that solar-plasma interaction can be effective enhancing solar thermochemical CO_2 decomposition processes while providing an approach to lessen the inherently intermittency of purely solar processes.

Further investigation of the solar-gliding arc plasma reactor using a structured experimentation approach (Design Of Experiments, DOE) has led to identify optimal operating conditions with potential to yield higher conversion and energy efficiencies. The implementation of the optimal conditions in the solar-gliding arc plasma reactor, expanding its application to three based cases of chemical processing targets, namely the decomposition of pure CO_2, and the processing of CO_2-CH_4 (4:1) and CO_2-H_2O mixtures, showed improved conversion of CO_2 of up to 5.77% with an energy efficiency of 22.3% at a lower specific energy input (SEI) of 3 kJ/l in the AXR reactor configuration. These improved results were achieved with CO_2-CH_4, which suggests the feasibility of the system for curbing CO_2 and CH_4 greenhouse gas emissions.

7.2. Key contributions

The most significant contributions of this research are the design, construction and characterization of a solar-gliding arc plasma reactor for gas-phase chemical synthesis, mainly for the decomposition of carbon dioxide, methane and other gases to reduce their emissions and at the same time provide solar fuels in a sustainable approach.

7.3. Recommendation for future work

Further investigation of the combined effects of solar photons and plasma-excited species on gas-phase chemical kinetics is required to understand the potential of the solar-glidarc approach to chemical synthesis.

In terms of electrode erosion, a detailed electrical characterization of the gliding arc in the presence of solar simulator is needed to understand the mechanism of electrical energy transfer during various states of the arc along the reactor. This will provide an important insight on how to address the erosion issues, which is particularly relevant when considering industrial implementations of the process.

Finally, investigating the phenomena related to solar energy absorption by nonequilibrium plasma is needed to understanding the potential synergy between solar photons and plasma electrons on chemical kinetics.

References

Abanades, S., & Chambon, M. (2010). CO2 dissociation and Upgrading from Two-step Solar thermochemical Processes Based on ZnO/Zn and SnO2/SnO Redox Pairs. Energy Fuels, 24, 6667–6674.

Abanades, S., Kimura, Hiroyuki, & Otsuka, Hiroyuki. (2014). Design and on-sun testing of a tube-type solar thermochemical reactor. Fuel Processing Technology, 122, 153-162.

Anderson, T.R., Hawkins, E., & Jones, P.D. (2016). CO_2 the greenhouse effect and global warming: from the pioneering work of Arrhenius and Callendar to today's Earth System Models. Endeavour, 40(3), 178-187 .

Bagotsky, V. S. (2006). Fundamentals of electrochemistry. New Jersey: John Wiley & Sons.

Bhatta, S., Nagassou, D., & Trelles, J. (2016). Solar photo-thermochemical reactor design for carbon dioxide processing. Solar Energy, 142, 253-266.

Bohmer, M., Langnickel, U., & Sanchez, M. (1991). Solar steam reforming of methane. Solar Energy Materials, 24, 441-448.

Bogaerts, A., Bie, D. C., Snoeckx, R., & Kozak, T. (2016). Plasma based CO_2 and CH_4 conversion: A modeling perspective. Plasma Processes and Polymers, 14.

Box, G. E. P., Hunter, W. G., & Hunter, J. S. (1978). An Introduction to Design, Data analysis, and Model Building. Toronto: John Wiley & Sons.

Burm, K. T. (2007). Calculation of the Townsend Discharge Coefficients and the Paschen Curve Coefficients. Contributions to Plasma Physics, 47(3), 177 – 182.

Chen, F. F. (2016). Introduction to Plasma Physics and Controlled Fusion. Springer International Publishing.

Chueh, W. C., Falter, C., Abbott, M., Scipio, D., Furler, P., Haile, S. M., and Steinfeld, A. (2010). High-flux solar-driven thermochemical dissociation of CO_2 and H_2O using nonstoichiometric ceria. Science, 330(6012), 1797-1801.

Da Silva, M. L. (n.d.). SPARTAN. Retrieved from http://esther.ist.utl.pt/spartan

Dassault Systèmes. (2016). SolidWorks: flow simulations

Edwards, J., Do, K., & Maitra, A. (1996). The use of solar-based CO_2/CH_4 reforming for reducing greenhouse gas emissions during the generation of electricity and process heat. Energy Conversion Management, 37, 1339-1344.

Fridman, A., & Kennedy, L. A. (2011). Plasma Physics and Engineering. Boca Raton: CRC Press.

Fridman, A., Nester, S., Kennedy, L. A., Saveliev, A., & Mutaf-Yardimci, O. (1999). Gliding arc gas discharge. Progress In Energy And Combustion Science, 25(2), 211-231.

Fridman, A. (2008). Plasma chemistry. New York: Cambridge University Press.

Froment, F. G., Bischoff, B. K., Wilde, D. J. (2011). Chemical Reactor Analysis and Design. New Jersey: John Wiley & Sons, Inc.

Fujishima, A., Rao, T. N., & Tryk, D. A. (2000). Titanium dioxide photocatalysis. Journal of Photochemistry and Photobiology, 1, 1-21.

Fuqiang, W., Ziming, C., Jianyu, T., Jiaqi, Z., Yu, L., & Linhua, L. (2017). Energy storage efficiency analyses of CO2 reforming of methane in metal foam solar thermochemical reactor. Applied Thermal Engineering, 111, 1091-1100.

Hirsch, D., & Steinfeld, A. (2004). Radiative transfer in a solar chemical reactor for the co-production of hydrogen and carbon by thermal decomposition of methane. Chemical Engineering Science, 59(24), 5771-5778.

Hirsch, D. & Steinfeld, A. (2004). Solar hydrogen production by thermal decomposition of natural gas   using a vortex-flow reactor. Hydrogen Energy, 29(1), 47-55.

Hori, Y., Murata, A., Kikuchi, K., & Suzuki, S. (1987). Electrochemical reduction of carbon dioxide to carbon monoxide at a gold electrode in aqueous potassium hydrogen carbonate. J. CHEM. SOC., CHEM. COMMUN.,, 1412, 728-729.

Information, A. E. (2018). Annual Energy Outlook.

Jin, T., Liu, C., & Li, G. (2014). Photocatalytic CO2 reduction using a molecular cobalt complex deposited on TiO2 nanoparticles. Royal Society of Chemistry, 50(47), 6221-6224 .

Kalra, C. S., Cho, Y. I., Gutsol, A., & Fridman, A. (2005). Gliding arc in tornado using a reverse vortex flow. Scientific Instruments, 76(2).

Kalra, C. S., Cho, Y. I., Gutsol, A., & Fridman, A. (2005). Gliding arc in tornado using a
    reverse-vortex flow. Review of Scientific Instruments, 76(2).

Kodama, T. (2003). High-temperature solar chemistry for converting solar heat to
    chemical fuels. Progress in Energy and Combustion Science, 29, 567-597.

Kogan, Abraham, and Meir Kogan. 2002. "The tornedo flow configuration - An effective
    method for screening of a solar reactor window." J. of Sol. Energy Eng 124(3),
    206-214.

Krueger, K., Davidson, J., & Lipinski, W. (2011). Design of a New 45 kW high-flux
    solar simulator for high-temperature solar thermal and thermochemical research.
    Solar Energy Engineering, 133(1).

Lapp, J., Davidson, J., & Lipinsky, W. (2011). Efficiency of two-step solar
    thermochemical non stoichiometric redox cycles with heat recovery. Energy,
    37(1), 591-600.

Liou, K. N. (2002). An Introduction to Atmospheric Radiation. Cambridge: Academic Press.

Liu, J.-L., Park, H.-W., Chung, W.-J., & Park, D.-W. (2016). High-efficient Conversion
    of CO2 in AC-Pulsed Tornado Gliding Arc PLasma. Plasma Chem Plasma
    Process, 36(2), 437–449.

Massarczyk, R., Chu, P., Elliott, S., Rielage, K., Dugger, C., & Xu, W. (2016, December
    20). arxiv. Retrieved August 8, 2018, from https://arxiv.org/pdf/1612.07170

Minitab 18 Statistical Software (2017). [Computer software]. State College, PA: Minitab,
Inc. (www.minitab.com)

Mohan, V. S., Velvizhi, J., Modestra, J. A., & Srikanth, S. (2014). Microbial fuel cell:
    Critical factors regulating bio-catalyzed electrochemical process and recent
    advancements. Renewable and Susatainable Energy Reviews, 40, 779-797.

Montgomery, D. C. (2012). Design and Analysis of Experiments. New Jersey: John
    Wiley & Sons.

Mutaf-Yardimci, O., Saveliev, A. V., Fridman, A. A., & Kennedy, L. A. (2000). Thermal
    and nonthermal regimes of gliding arc discharge in air flow. Journal of Applied
    Physics, 87(4), 1632-1641.

Nagassou, D., Mohsenian, S., Elahi, R., & Trelles, J. P. (2017). On the Potential for
Enhancement of Solar Thermochemcial Synthesis Processes by Nonequilibrium
Plasma. American Institute of Chemical Engineers. Minneapolis.

Nunnally, T., Gutsol, K., Rabinovich, A., Fridman, A., Gutsol, A., & Kemoun, A. (2011).
Dissociation of CO2 in a low current gliding arc plasmatron. Journal of Physics
D: Applied Physics, 44, 274009-274016.

Oturan, M. A. (2014). Electrochemical advanced oxidation technologies for removal of
organic pollutants in water. Environ Sci Pollut Res, 21(14), 8333–8335.

Ozalp, N., & Shilapuram, Vidyasagar. (2010). Step-by-step methodology of developing a
solar reactor for emission-free generation of hydrogen. Hydrogen Energy, 35(10),
4484-4495.

Ozalp, N., Kogan, A., & Epstein, M. (2009). Solar decomposition of fossil fuels as an
option for sustainability. Hydrogen Energy, 34(2), 710-720.

Parent, Y., Blake, D., Magrini-Bair, K., Lyons, C., Turchi, C., Watt, A., . . . Prairie, M.
(1996). Solar photocatalytic processes for the purification of water: state of
development and barriers to commercialization. Solar Energy, 56(5), 429-437.

Roy, S. C., Varghese, O. K., Paulose, M., & Grimes, C. A. (2010). Towards Solar Fuels:
Photocatalytic Conversion of Carbon Dioxide to Hydrocarbons. American
Chemical Society, 4(3), 1259–1278.

Salameh, Z. (2014). Global Warming And Renewable Energy Use. In Renewable Energy
System Design (pp. 22-23). Waltham: Academic Press.

Shen, J., Kortlever, R., Kas, R., Birdja, Y. Y., Diaz-Morales, O., Kwon, Y., . . . Koper,
M. T. (2015). Electrocatalytic reduction of carbon dioxide to carbon monoxide
and methane at an immobilized cobalt protoporphyrin. nature communications, 6.

Solomon, S., Plattner, G.-K., Knutti, R., & Friedlingstein, P. (2009, February 10). The
National Academic of Sciences of the USA. Retrieved August 2018, from
www.pnas.org/cgi/doi/10.1073/pnas.0812721106

Steinfeld, A. (2005). Solar thermochemical production of hydrogen - a review. Solar
Energy, 78(5), 603-615.

Steinfeld, A., Brack, M., Meier, A., Weidenkaff, A., & Wuillemin, D. (1998). A solar chemical reactor for the co-production of zinc and synthesis gas. Energy, 23(10), 803-814.

Taguchi, G. (1987). System of Experimental Design. New Jersey: Quality Resources.

Taylan, O., & Berberoglu, H. (2013). Discharge of Carbon Dioxide Using A Non-Thermal Plasma Reactor. American Society of Mechanical Engineers. Minneapolis.

Wei, Z., Liu, D., Hsu, C., & Liu, F. (2014). All-vanadium redox photoelectrochemical cell: An approach to store solar energy. Electrochemistry Communications, 45, 79-82.

List of publications

Refereed journals/Conference proceedings

- S. Bhatta, **D. Nagassou**, J. P. Trelles, "Solar Photo-Thermochemical Reactor Design for Carbon Dioxide Processing", Solar Energy (2017), Vol. 142, pp. 253–266. DOI: 10.1016/j.solener.2016.12.031

- S. Bhatta, **D. Nagassou**, J. P. Trelles, "Direct Receiver-Reactor for Solar Photo-Thermochemical Processing", 2015 ASME Power & Energy Conference, ASME 2015 9th International Conference on Energy Sustainability, San Diego, California, June 28 – July 2, 2015.

- S. Bhatta, **D. Nagassou**, J. P. Trelles, "High-Flux Solar Simulator and Solar Photo-Thermal Reactor: Design and Analysis", ASME 8th International Conference on Energy Sustainability, Boston, Massachusetts, June 30 – July 2, 2014.

- **D. Nagassou**, S. Mohsenian, R. Elahi, J. P. Trelles, "On the Potential for Enhancement of Solar Thermochemical Synthesis Processes by Nonequilibrium Plasma", Annual Meeting of the American Institute of Chemical Engineers (2017 AIChE Annual Meeting) - Symposium on Solar Power and Chemical Systems in Honor of Prof. Edward A. Fletcher, Minneapolis, Minnesota, Oct. 29 – Nov. 3, 2017.

- **D. Nagassou**, S. Mohsenian, S. Bhatta, J. P. Trelles, "Solar-Plasma Reactor: Characterization and Design", 2017 Fulbright Enrichment Seminar on Climatic Impacts, May 17 – 21, Denver, CO.

- S. Bhatta, **D. Nagassou**, R. O. Castro, J. P. Trelles, "SOLAR Chemical Synthesis: From CO2 to Fuels", 17th Annual student Research Symposium, University of Massachusetts Lowell, Lowell, MA, April 22, 2014. Best Poster Award

- S. Mohsenian, S. Sheth, S. Bhatta, **D. Nagassou**, D. Sullivan, J. P. Trelles, "Design and characterization of an electromagnetic-resonant cavity microwave plasma reactor for

atmospheric pressure carbon dioxide decomposition", Plasma Processes and Polymers DOI: 10.1016/j.solener.2016.12.031

- S. Bhatta, **D. Nagassou,** S. Mohsenian, J. P. Trelles, "Solar Photo-Thermochemical Decomposition of Carbon Dioxide in a Direct Solar Receiver Reactor at Atmospheric Pressure", Solar Energy (2018)

- **D. Nagassou,** S. Mohsenian, S. Bhatta, R. Elahi, J. P. Trelles, "Solar – gliding arc plasma reactor for carbon dioxide decomposition: design and characterization" (submitted November 2018)